

Black Hole Mass Gap: A Writeup

Vaishnav V. Rao, Harshda Saxena

November 28, 2021

Contents

1	Introduction	4
1.1	Context	4
1.2	The discovery of GW190521	4
1.3	Organization of the writeup	4
2	Stellar evolution, dynamical instability, PPI, BH formation	5
2.1	Stellar Structure - A theoretical preview [4]	5
2.1.1	The first 2 stellar equations	5
2.1.2	The main sources of Energy	6
2.1.3	Energy Transport Mechanisms	8
2.1.4	Building a stellar model	9
2.1.5	Polytropes and the Lane Emden equations	10
2.1.6	The Eddington Standard Model	11
2.1.7	Evolution on the main sequence	11
2.1.8	Evolution off the main sequence	13
2.2	Dynamical Instability	16
2.2.1	One-zone model [4]	16
2.2.2	Homologous model	17
2.3	Pair-instability	18
2.4	Oxygen ignition	20
2.5	Core Collapse Supernova [4]	20
2.6	How Massive Single Stars End their Life [15]	22
2.6.1	Remnant properties	23
3	The Black Hole Mass gap	24
3.1	Known Physics Dependence of the BHMg [10]	26
3.1.1	Metallicity	26
3.1.2	Wind Mass Loss	28
3.2	Nuclear Physics	29
3.3	Neutrino losses	30
3.3.1	Convective mixing	31
3.4	Effect of novel particle emissions	32
3.4.1	General Effects	33
3.4.2	Energy Loss Contours	33
3.4.3	MESA results from [7]	34

3.4.4	Massive novel particle production	35
4	MESA implementation (overview of MESA)[28]	36
4.1	Implementation of HLLC	36
4.2	Energy Accounting in MESA	38
4.2.1	Fundamental equations	38
4.2.2	Implementation in MESA	39
4.2.3	Relationship to the Riemann Solver-Based Hydrodynamics Implementation	39
5	MESA software	40
5.1	Installation procedure	40
5.2	Importing and running the testsuite	41
5.3	A small introduction to the different files	41
5.4	Installing on cluster	42
5.5	Running MESA jobs on cluster	42
5.5.1	Single Jobs	42
5.5.2	Many Jobs	43
5.6	Storage of MESA data	44
5.7	Extracting data using PyMESARReader	45
6	Different stages in MESA important for PPISN	45
6.1	Introduction to the PPISN testsuite	45
6.2	Pulsation evolution using HLLC	46
7	Reproduced figures	46
7.1	Lower edge of the mass gap	46
7.2	Miscellaneous plots	48
7.3	Attempt at the instability region	49
7.3.1	Thermodynamics	49
7.3.2	Ions	50
7.3.3	Radiation	50
7.3.4	Electrons and Positrons	50
7.3.5	Attempt on Mathematica	51
8	Literature survey	51
8.1	Astrophysics papers	51
8.1.1	Accretion in Binaries [37]	51
8.1.2	Astrophysical Implications of GW190521 [1]	51
8.1.3	Formation of Binary Black Holes Similar to GW190521 [17]	52
8.1.4	BH population analysis [2]	52
8.1.5	Collisions & BHMG [19]	52
8.1.6	Convection dependence of BHMG [30]	53
8.1.7	Core collapse after PPISN [29]	53
8.1.8	Effect of Overshoot on BHMG [35][36]	53
8.1.9	Effect of Reaction Rates on BHMG [6]	54
8.1.10	Effect of Rotation on BHMG [24]	54
8.1.11	Helium Burning and CO reaction rates [9]	55
8.1.12	Likelihood of GW190521 under mass and spin priors [27]	55
8.1.13	Max BH mass across cosmic time [38]	55

8.1.14	Modified Gravity and BHMG [33]	56
8.1.15	PBH and BHMG [8]	56
8.1.16	Pulsational Pair-instability Supernovae, Pre-collapse Evolution and Pulsational Mass Ejection [23]	57
8.1.17	PPISN-Astrophysics [39]	57
8.1.18	Rotation, binaries, accretion-BHMG [40]	58
8.1.19	GW190521 as a statistical outlier [26]	58
8.1.20	GW190521 as a straddling binary [12]	59
8.2	Particle Physics Papers	59
8.2.1	Beyond the Standard Model Explanations of GW190521 [31]	59
8.2.2	Effect of Non-Nuclear Energy on BHMG [42]	60
8.3	Miscellaneous Papers	60
8.3.1	Core-Collapse Supernovae from 9 to 120 Solar Masses Based on Neutrino-powered Explosions [34]	60
8.3.2	Constraints on Core Collapse from the Black Hole Mass function[18]	60
8.3.3	How Massive Single Stars End their Life [15]	61
8.3.4	Effect of PI Mass Loss on Mergers[3]	61
8.3.5	Observational constraints on the progenitors of core-collapse supernovae : the case for missing high mass stars[32]	61
8.3.6	Progenitor Mass Distribution of Core-Collapse Supernova Remnants in Our Galaxy and Magellanic Clouds based on Elemental Abundances [16]	62
8.3.7	Stellar Collapse Diversity and the Diffuse Supernova Neutrino Background [20]	62
8.3.8	The Black Hole formation probability[5]	63
8.3.9	The Search for Failed Supernovae with The Large Binocular Telescope: First Candidates[13]	64
8.3.10	The Deaths of Very Massive Stars[41]	64

1 Introduction

1.1 Context

The existence of the BHMG stems from pair-instability encountered during the carbon burning phase (post hydrogen burning main sequence phase and helium burning phase) of massive, low metallicity population-III stars towards the end of their life cycle. This is spurred by the production of non-relativistic electron-positron pairs in the cores. The pair production reduces the radiation pressure such that it no longer supports the star against gravitational collapse. The resulting contraction and temperature rise leads to rapid thermonuclear burning of ^{16}O , which may release an amount of energy comparable to the star’s binding energy. The strength of the explosion and subsequent evolution is highly dependent on the mass and metallicity of the parent star.

Lighter progenitors (He core mass $\sim 50 - 90M_{\odot}$ for metallicity $Z \sim 10^{-3}$) usually undergo one or more pulses which shed mass. This has led them to be referred to as pulsational pair-instability supernovae (PPISN). Eventually, these stars return to hydrostatic equilibrium and ultimately core collapse, but the resulting black holes are significantly lighter than they would have been in the absence of pair instability. The greatest BH mass before pair-instability effects become significant determines the lower edge of the mass gap. Heavier progenitors ($\gtrsim 90M_{\odot}$ for $Z \sim 10^{-3}$) undergo such a violent explosion that no remnant is left at all, and are referred to as pair-instability supernova (PISN). In very heavy progenitors ($\gtrsim 240M_{\odot}$ for $Z \sim 10^{-3}$) pair instability is quenched as some of the energy from contraction is used to photodisintegrate heavy elements. The lightest black hole formed from this process defines the upper edge of the mass gap.

1.2 The discovery of GW190521

On May 21, 2019, Advanced LIGO and Advanced Virgo observed a short duration gravitational-wave signal, GW190521. If GW190521 is from a quasicircular binary inspiral, then the detected signal is consistent with the merger of two black holes with masses of $85M_{\odot}$ ($+21, -14M_{\odot}$) and $66M_{\odot}$ ($+17, -18M_{\odot}$) (90 % credible intervals) [1]. They thus infer that the primary black hole mass lies within the gap produced by (pulsational) pair-instability supernova processes. [14] also report the first plausible optical electromagnetic counterpart to a (candidate) binary black hole merger. They postulate that the electromagnetic flare is consistent with expectations for a kicked binary black hole merger in the accretion disk of an active galactic nucleus.

Due to the context as given above, this discovery placed the 2 BH masses bang in the middle of the BHMG due to PI, and there have been multiple attempts to explain this mismatch between theory and prediction, from purely astrophysical explanations to BSM explanations and Modified Gravity theories. We mainly follow in the steps of [10] and [7] to reproduce some of their results.

1.3 Organization of the writeup

In Section 2 we start with a theoretical preview of stellar structure (mainly following [4]), helium burning, the derivation of the dynamical instability, the derivation of instability region equations, the reason, reactions, and effects of pair instability, the instability region plot and explanation (following [7]), a description of pulsations following O ignition, description of core collapse and finally BH formation.

In Section 3 we explain the death of star processes at different mass ranges, specifically focusing

on the PISN, thereby spelling out the mass gap. We then explain the known physics dependence: metallicity, C/O reaction rates, wind mass loss, neutrino losses, convective mixing (from [10]) and BSM explanations of novel particles: electrophilic axions, photophilic axions, massive particles, and hidden photons (from [7]).

In Section 4 we explain the numerical modelling of stellar structure and stellar equations in the 1D stellar evolution code MESA, and give a small description of the main libraries used by MESA (mainly following [28]).

In Section 5 we begin with the installation procedure for MESA, the process of importing and running test suites which exist by default in MESA, which files in MESA perform which functionalities, the process of installing and running MESA on a cluster, specifically running single jobs, structuring inlists, and running many jobs. We also describe the storage of MESA data and the way we can extract data using PyMESARReader to analyze the data in Python.

In Section 6 we begin by describing the PPISN test suite, the evolution of pulses using HLLC, including the criteria to switch to a hydrodynamic solver during certain parts of the star evolution.

In Section 7 we present our final reproduced results obtained after running MESA on cluster, and the conditions that we use for He depletion, CO-core mass, Fe-core-infall, and the final BH criteria. We also put our reproduced figures of the HR Diagram (for practice), the plot for the mass of the BH, He mass, CO core mass versus the ZAHB mass, our attempt at the central T-Rho plane instability region, the mass loss during pulsations as a function of core temperature, and the Webplotdigitizer comparison of our final plot with [7].

We finally present some of our key references and summaries of other major work done in this area under Section 8.

2 Stellar evolution, dynamical instability, PPI, BH formation

2.1 Stellar Structure - A theoretical preview [4]

2.1.1 The first 2 stellar equations

The gravitational force is always attractive, implying that an opposing force must exist if a star is to avoid collapse. This force is provided by pressure. Assume there are no shear stresses, on a cylinder of dm mass. Assuming these are the only forces on the cylinder, assuming spherical symmetry and that the star is static, we get the condition of hydrostatic equilibrium as -

$$\frac{dP}{dr} = -G \frac{M_r \rho}{r^2} = -\rho g \quad (1)$$

in order for a star to be static, a pressure gradient dP/dr must exist to counteract the force of gravity. It is not the pressure that supports a star, but the change in pressure with radius. There is also the mass conservation equation -

$$\frac{dM_r}{dr} = 4\pi r^2 \rho \quad (2)$$

The pressure integral computes the pressure given a distribution function of momenta, which can be converted to one in velocity (for massive particles, non relativistic in an ideal gas). This is given as -

$$P = \frac{1}{3} \int_0^\infty n_p p v dp \quad (3)$$

$$n_v dv = n \left(\frac{m}{2\pi kT} \right)^{3/2} e^{-\frac{mv^2}{2kT}} 4\pi v^2 dv \quad (4)$$

where n is the particle number density.

For a variety of masses, we get $P_g = \rho kT / \mu m_H$, where $\mu = \rho / n m_H$, the mean molecular weight. The mean molecular weight depends on the composition of the gas as well as on the state of ionization of each species. The level of ionization enters because free electrons must be included in the average mass per particle m . For a neutral gas

$$\frac{1}{\mu_n} = X + \frac{Y}{4} + \left\langle \frac{1}{A_n} \right\rangle Z$$

Here, $\langle 1/A_n \rangle$ is the weighted average of all elements in the gas heavier than helium, where X , Y and Z are the mass fractions of hydrogen, helium and metals respectively. Similarly, for a completely ionized gas, we use

$$\frac{1}{\mu_i} = \sum_i \frac{1 + z_i}{A_i} X_i$$

where z is the number of free electrons. From these, we also get the average kinetic energy per particle as $1/2 m \bar{v}^2 = 3/2 kT$ ($1/2 kT$ per degree of freedom). This is the Maxwell-Boltzmann statistics, however, Fermi-Dirac distribution function incorporates quantum mechanics and leads to different equations for fermions. Similarly, bosons follow the Bose-Einstein statistics. Finally, we combine the radiation pressure, which using the Planck distribution function, comes as

$$P_{rad} = \frac{aT^4}{3}$$

where a is the radiation constant.

2.1.2 The main sources of Energy

Taking ϵ to be the total energy released per kg per second, we get -

$$\frac{dL_r}{dr} = 4\pi r^2 \rho \epsilon \quad (5)$$

where L_r is the total luminosity up to a radius r .

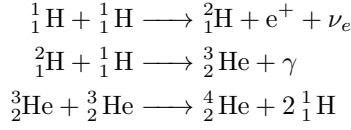
During every nuclear reaction it is necessary to conserve electric charge, the number of nucleons, and the number of leptons.

Proton-Proton Chains -

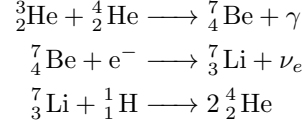
Applying the conservation laws, one chain of reactions that can convert hydrogen into helium is the first proton-proton chain (PPI). The ultimate reaction is -



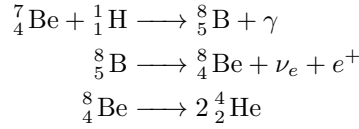
With the intermediate steps being -



The initial step is the slowest, requiring the decay of a proton to a neutron using the weak force. 31% of the time, in the second step the PPII chain occurs -

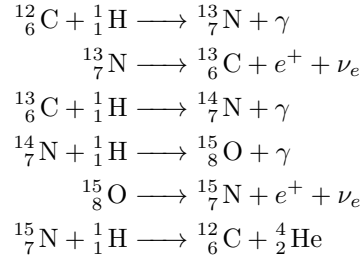


Only a 0.3% of the time, a PP III chain occurs -

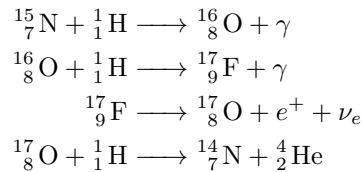


CNO cycle -

In the CNO cycle, carbon, nitrogen, and oxygen are used as catalysts, being consumed and then regenerated during the process. The first branch is -



thus effectively producing He from H. The second branch arises with a probability of 0.04% , with the last step changed -

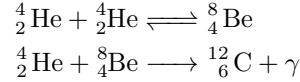


The CNO cycle is much more strongly temperature-dependent than the pp chain. This property implies that low-mass stars, which have smaller central temperatures, are dominated by the pp chains during their “hydrogen burning” evolution, whereas more massive stars, with their higher central temperatures, convert hydrogen to helium by the CNO cycle. When hydrogen is converted into

helium by either the pp chain or the CNO cycle, the mean molecular weight of the gas increases. If neither the temperature nor the density of the gas changes, the ideal gas law predicts that the central pressure will necessarily decrease. As a result, the star would no longer be in hydrostatic equilibrium and would begin to collapse. This collapse has the effect of actually raising both the temperature and the density to compensate for the increase in μ .

Triple Alpha Process -

The reaction sequence by which helium is converted into carbon is known as the triple alpha process. It is given by -



This process exhibits a very strong temperature dependence (T^{41}).

Carbon and Oxygen burning -

After sufficient carbon has been generated by the triple alpha process, it becomes possible for carbon nuclei to capture alpha particles, producing oxygen. Some oxygen captures alpha particles to form neon. If the star is very massive, higher temperatures result in carbon burning (forming O, Na, Ne and Mg) and oxygen burning reactions (forming Mg, Si, P and S).

Checking the Binding Energy per nucleon $E_b/A = [Zm_p + (A - Z)m_n - m_{\text{nucleus}}]c^2/A$, the most stable nuclei (called magic nuclei) are H, He, O, C, Ne, N, Mg, Si and Fe, whose isotopes have the same number of protons and neutrons (except ${}^{56}_{26}\text{Fe}$).

2.1.3 Energy Transport Mechanisms

Three different energy transport mechanisms operate in stellar interiors. Radiation allows the energy produced by nuclear reactions and gravitation to be carried to the surface via photons. Convection can be a very efficient transport mechanism in many regions of a star, with hot, buoyant mass elements carrying excess energy outward while cool elements fall inward. Finally, conduction transports heat via collisions between particles. Although conduction can play an important role in some stellar environments, it is generally insignificant in most stars throughout the majority of their lifetimes.

Radiative Transport -

The temperature gradient for radiative transport is -

$$\frac{dT}{dr} = -\frac{3\bar{\kappa}\rho L_r}{4acT^3 4\pi r^2} \quad (7)$$

If the temperature gradient becomes too steep, convection can begin to play an important role in the transport of energy. Physically, convection involves mass motions: hot parcels of matter move upward as cooler, denser parcels sink. Turbulent flows emerge, and require detailed viscosity and heat dissipation knowledge. Convection is strongly coupled to the stars behaviour.

Convective Transport -

To estimate the size of a convective region in a star, consider the pressure scale height, H_p defined as

$$\frac{1}{H_p} = -\frac{dP}{Pdr} \quad (8)$$

Using the pressure gradient equation

$$H_p = \frac{P}{\rho g} \quad (9)$$

The first law of thermodynamics gives us $dQ = dU + dW$, where U , the internal energy of a system is a state function and dQ and dW are inexact differentials. The specific heat (at constant pressure and volume) is defined as the amount of heat required to raise the temperature of unit mass of a material by a unit temperature interval, $C_P = (\partial Q / \partial T)|_P$ and $C_V = (\partial Q / \partial T)|_V$. We get for a monoatomic gas, $C_V = 3/2 nR$ and always $C_P = C_V + nR$. The adiabatic index γ is defined as C_P / C_V . As both the specific heats increase, γ approaches unity. The adiabatic gas law is given as $PV^\gamma = \text{const}$. The sound speed is defined as $v_s = \sqrt{B/\rho}$, where $B = -V \partial P / \partial V$. With this, the adiabatic sound speed becomes $v_s = \sqrt{\gamma P / \rho}$.

In convection, we first consider the situation where a hot convective bubble of gas rises and expands adiabatically. After it has traveled some distance, it finally thermalizes, giving up any excess heat as it loses its identity and dissolves into the surrounding gas. Using the equation for adiabatic expansion, and assuming that μ is a constant, we get -

$$\left. \frac{dT}{dr} \right|_{ad} = - \left(1 - \frac{1}{\gamma} \right) \frac{\mu m_H G M_r}{k r^2} = - \frac{g}{C_p} \quad (10)$$

In general, convection will occur when -

- the stellar opacity is large, implying that an unachievably steep temperature gradient would be necessary for radiative transport
- a region exists where ionization is occurring, causing a large specific heat and a low adiabatic temperature gradient
- the temperature dependence of the nuclear energy generation rate is large, causing a steep radiative flux gradient and a large temperature gradient.

In the atmospheres of many stars, the first two conditions can occur simultaneously, whereas the third condition would occur only deep in stellar interiors. In particular, the third condition can occur when the highly temperature-dependent CNO cycle or triple alpha processes are occurring. The mixing length is the point at which it thermalizes with its surroundings, giving up its excess heat at constant pressure, and is given by $l = \alpha H_p$.

2.1.4 Building a stellar model

The static stellar equations are as summarized below -

$$\begin{aligned} \frac{dP}{dr} &= -G \frac{M_r \rho}{r^2} \\ \frac{dM_r}{dr} &= 4\pi r^2 \rho \\ \frac{dL_r}{dr} &= 4\pi r^2 \rho \epsilon \\ \frac{dT}{dr} &= - \frac{3\bar{\kappa} L_r}{4acT^3 4\pi r^2} \quad (\text{radiation}) \\ &= - \left(1 - \frac{1}{\gamma} \right) \frac{\mu m_H G M_r}{k r^2} \quad (\text{adiabatic convection}) \end{aligned}$$

These require information concerning the physical properties of the matter from which the star is made. The required conditions are the equations of state of the material and are collectively referred to as constitutive relations. Specifically, we need relationships for the pressure, the opacity, and the energy generation rate, in terms of fundamental characteristics of the material: the density, temperature, and composition. The pressure equation of state, including ideal gas and radiation pressure, works well enough. The opacity is calculated for different regions at specific compositions, densities and temperatures. For energy generation we use the pp chain and the CNO cycle. The boundary conditions imply $M_r, L_r = 0$ as $r = 0$, and $T, \rho, P = 0$ as $r=R$.

The Vogt-Russell theorem states that : The mass and the composition structure throughout a star uniquely determine its radius, luminosity, and internal structure, as well as its subsequent evolution, and is the philosophy on which modelling is based on.

2.1.5 Polytropes and the Lane Emden equations

Hypothetical stellar models in which the pressure depends on density in the form $P = K\rho^\gamma$ are known as polytropes. From the hydrostatic equilibrium case, take ρ and r^2 to the other side, and take a radial derivative to get -

$$\frac{d}{dr} \left(\frac{r^2 dP}{\rho dr} \right) = -G \frac{dM_r}{dr}$$

Using the second stellar equation to eliminate M_r , we get -

$$\frac{1}{r^2} \frac{d}{dr} \left(\frac{r^2 dP}{\rho dr} \right) = -4\pi G \rho$$

This is actually a slightly camouflaged form of a very well-studied differential equation known as Poisson's equation. We now employ the relationship $P(\rho) = K\rho^\gamma$, where K and $\gamma > 0$ are constants. This functional form of the pressure equation is known generally as a polytropic equation of state. Using the scaled form of the pressure and density - $P = K\rho_c^{1+\frac{1}{n}}\theta^{n+1}$ and $\rho = \rho_c\theta^n$, we get

$$\frac{1}{r^2} \frac{d}{dr} \left(r^2 K \rho_c^{\frac{1}{n}} (n+1) \frac{d\theta}{dr} \right) = -4\pi G \rho_c \theta^n$$

Substituting $r = \alpha\xi$, with $\alpha^2 = (n+1)K\rho_c^{\frac{1}{n}-1}/4\pi G$. We finally have the Lane-Emden equation -

$$\frac{1}{\xi^2} \frac{d}{d\xi} \left(\xi^2 \frac{d\theta}{d\xi} \right) + \theta^n = 0$$

We use separation of variables as -

$$\frac{dy}{d\xi} = \frac{z}{\xi^2} \frac{dz}{d\xi} = -\xi^2 y^n$$

Subject to the boundary conditions of -

- $\theta(0) = 1$, as the central density is just ρ_c , that is, $y(0) = 1$
- $\frac{d\theta}{d\xi}|_{\xi=0} = 0$, that is, $z(0)$ is approx 0.

2.1.6 The Eddington Standard Model

This model is associated with a star in radiative equilibrium.

Let the fraction of pressure due to ideal gas be some β , which in general can be a function of temperature and density, but we assume it to be a constant for this simplistic derivation. Hence we have the 2 pressure equations to be -

$$\begin{aligned}\beta P &= \frac{\rho k T}{\mu m_H} \\ (1 - \beta)P &= \frac{a T^4}{3}\end{aligned}$$

Solving these 2, we end up with -

$$P = \left(\frac{3(1 - \beta)K^4}{a\beta^4\mu^4 m_H^4} \right)^{1/3} \rho^{4/3}$$

Comparing this with the polytropic equation, this implies $n=3$ for the Eddington Standard Model.

2.1.7 Evolution on the main sequence

The existence of the main sequence is due to the nuclear reactions that convert hydrogen into helium in the cores of stars. The timescale of nuclear reactions is the largest, which governs the life on the main sequence compared to the Kelvin-Helmholtz timescale (timescale of radiating the gravitational binding energy) or the free fall timescale.

Low mass main sequence evolution Zero Age Main Sequence (ZAMS) stars with masses more than 1.2M have convective cores due to the highly temperature-dependent CNO cycle. On the other hand, ZAMS stars with masses less than 1.2 M are dominated by the less temperature dependent pp chain. This implies that ZAMS stars in the range 0.3 M to 1.2 M possess radiative cores. However, the lowest-mass ZAMS stars again have convective cores because their high surface opacities drive surface convection zones deep into the interior, making the entire star convective.

The evolution on the main sequence occurs because, as the pp chain converts hydrogen into helium, the mean molecular weight μ of the core increases. According to the ideal gas law, unless the density and/or temperature of the core also increases, there will be insufficient gas pressure to support the overlying layers of the star. As a result, the core must be compressed. While the density of the core increases, gravitational potential energy is released, and, as required by the virial theorem, half of the energy is radiated away and half of the energy goes into increasing the thermal energy and hence the temperature of the gas. One consequence of this temperature increase is that the region of the star that is hot enough to undergo nuclear reactions increases slightly during the main-sequence phase of evolution. This also leads to increase in T and ρ of the core, increasing the luminosity of the star (by increase of both T and R).

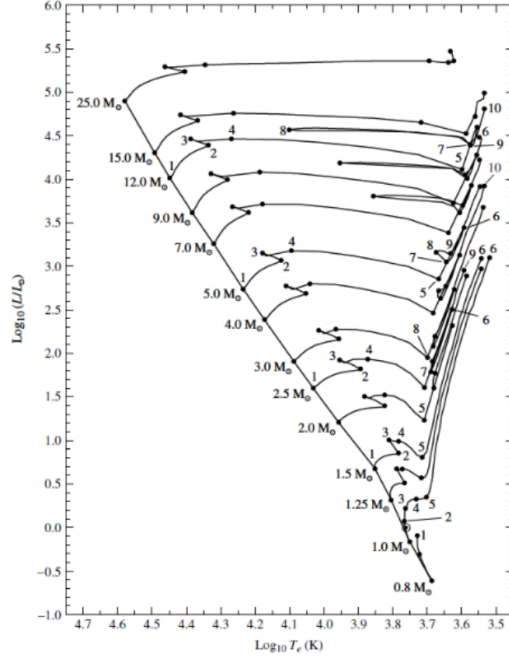


Figure 1: Main-sequence and post-main-sequence evolutionary tracks of stars with a predetermined initial composition. The model calculations include mass loss and convective overshooting. The diagonal line connecting the locus of points 1 is the zero-age main sequence.

With the depletion of hydrogen in the core, the generation of energy via the pp chain must stop. However, by now the core temperature has increased to the point that nuclear fusion continues to generate energy in a thick hydrogen-burning shell around a small, predominantly helium core. For an isothermal core to support the material above it in hydrostatic equilibrium, the required pressure gradient must be the result of a continuous increase in density as the center of the star is approached. At this point, the luminosity being generated in the thick shell actually exceeds what was produced by the core during the phase of core hydrogen burning. As a result, the evolutionary track continues to rise. As the envelope of the star expands, the effective temperature begins to decrease slightly and the evolutionary track bends to the right. As the hydrogen-burning shell continues to consume its nuclear fuel, the ash from nuclear burning causes the isothermal helium core to grow in mass while the star moves farther to the red in the H-R diagram.

As the core mass increases, the maximum pressure at the surface of the core decreases. At some point, it may no longer be possible for the core to support the overlying layers of the star's envelope. This phase of evolution ends when the mass of the isothermal core has become too great and the core is no longer capable of supporting the material above it. The maximum fraction of a star's mass that can exist in an isothermal core and still support the overlying layers is given by -

$$\left(\frac{M_{ic}}{M}\right) = 0.37 \left(\frac{\mu_{env}}{\mu_{ic}}\right)^2 \quad (11)$$

where env and ic stand for the envelope and isothermal core respectively, and this is known as the Schönberg-Chandrasekhar limit. When the mass of the isothermal helium core exceeds this limit,

the core collapses on a Kelvin–Helmholtz timescale, and the star evolves very rapidly relative to the nuclear timescale of main-sequence evolution. For stars below about 1.2 M, this defines the end of the main-sequence phase.

The mass of an isothermal core may exceed the Schönberg–Chandrasekhar limit if an additional source of pressure can be found to supplement the ideal gas pressure. This can occur if the electrons in the gas start to become degenerate. With increasing density, the electrons in the gas are forced to occupy the lowest available energy levels. Obeying the Pauli Exclusion Principle, electrons are stacked into progressively higher states, and in complete degeneracy, the pressure becomes independent of temperature, and is given by $P = K\rho^{5/3}$, in the non relativistic case.

Main sequence evolution of massive stars The evolution of more massive stars on the main sequence is similar to that of their lower-mass cousins with one important difference: the existence of a convective core, mixing the material and keeping it homogeneous, since the convection time scale is much lesser than the nuclear timescale. Moving up the main sequence, as the star evolves the convection zone in the core retreats more rapidly with increasing stellar mass, disappearing entirely before the hydrogen is exhausted for those stars with masses greater than about 10 M. When the mass fraction of hydrogen reaches about $X = 0.05$ in the core of a 5 M star, the entire star begins to contract. With the release of some gravitational potential energy, the luminosity increases slightly. Since the radius decreases, the effective temperature must also increase. For stars with masses greater than 1.2 M, this stage of overall contraction is defined to be the end of the main-sequence phase of evolution.

2.1.8 Evolution off the main sequence

The Subgiant Branch For both low- and intermediate-mass stars, the shell continues to consume the hydrogen that is available at the base of the star’s envelope, increasing the mass of the helium core till it reaches the above limit. The core begins to contract rapidly, causing the evolution to proceed on the much faster Kelvin–Helmholtz timescale. The gravitational energy released by the rapidly contracting core again causes the envelope of the star to expand and the effective temperature cools, resulting in redward evolution on the H–R diagram. This phase of evolution is known as the subgiant branch (SGB). As the core contracts, the temperature and density of the hydrogen-burning shell increases, and, although the shell begins to narrow significantly, the rate at which energy is generated by the shell increases rapidly.

Red Giant Branch With the expansion of the stellar envelope and the decrease in effective temperature, the photospheric opacity increases due to the additional contribution of the H^- ion. The result is that a convection zone develops near the surface for both low- and intermediate-mass stars. With the nearly adiabatic temperature gradient associated with convection throughout much of the stellar interior, and the efficiency with which the energy is transported to the surface, the star begins to rise rapidly upward along the red giant branch (RGB) of the H–R diagram. When these convection zones reach deep enough into the chemically modified regions, observable changes occur in the photosphere, decrease in Li and increase in 3-He. This transport of materials from the deep interior to the surface is referred to as the first dredge-up phase. At the tip of the RGB, temperatures and densities of the core have become high enough to initiate triple alpha burning, also converting to O. With the onset of a new and strongly temperature-dependent source of energy, the core expands, cooling it, abruptly decreasing the luminosity. The envelope contracts and the T starts increasing.

Helium Core Flash The evolution changes for stars lesser than 1.8M here. Significant neutrino losses from the core of the star prior to reaching the tip of the RGB result in a negative temperature gradient near the center (i.e., a temperature inversion develops); the core is actually refrigerated somewhat because of the energy that is carried away by the neutrinos. When the temperature and density become high enough to initiate the triple alpha process, the ensuing energy release is almost explosive. The ignition of helium burning occurs initially in a shell around the center of the star, but the entire core quickly becomes involved and the temperature inversion is lifted, resulting in an very short energy burst, and is absorbed by the overlying layers, known as the helium core flash. The origin of the explosive energy release is in the very weak temperature dependence of electron degeneracy pressure and the strong temperature dependence of the triple alpha process.

Horizontal Branch For both low- and intermediate-mass stars, as the envelope of the model contracts following the red giant tip, the increasing compression of the hydrogen-burning shell eventually causes the energy output of the shell, and the overall energy output of the stars, to begin to rise again. With the associated increase in effective temperature, the deep convection zone in the envelope rises toward the surface, while at the same time, a convective core develops. The appearance of a convective core is due to the high temperature sensitivity of the triple alpha process. This generally horizontal evolution is the blueward portion of the horizontal branch (HB) loop. The redward portion starts after the end, due to the increase in μ of the core, causing it to contract.

With the increase in core temperature associated with its contraction, a thick helium burning shell develops outside the CO core. As the core continues to contract, the helium burning shell narrows and strengthens, forcing the material above the shell to expand and cool. This results in a temporary turn-off of the hydrogen-burning shell.

Asymptotic Giant Branch When the redward evolution reaches the Hayashi track, the evolutionary track bends upward along a path referred to as the asymptotic giant branch (AGB). The AGB may be thought of as the helium-burning-shell analog to the hydrogen-burning-shell RGB. The expanding envelope initially absorbs much of the energy produced by the helium burning shell. As the effective temperature continues to decrease, the convective envelope deepens again, this time extending downward to the chemical discontinuity between the hydrogen-rich outer layer and the helium-rich region above the helium-burning shell. The mixing that results during this second dredge-up phase increases the helium and nitrogen content of the envelope. This is the early phase.

Near the upper portion of the AGB, the dormant hydrogen-burning shell eventually reignites and again dominates the energy output of the star. However, during this phase of evolution, the narrowing helium burning shell begins to turn on and off quasi-periodically, due to the dumping of helium ash. This leads to the helium shell flash, turning off hydrogen shell for a while. This leads to thermal pulses.

In the third dredge up phase, the carbon-rich material is brought to the surface, decreasing the ratio of oxygen to carbon, after a helium flash due to convective zones in intermediate mass stars.

Mass Loss and AGB evolution AGB stars lose mass at a rapid rate, hence dust grains tend to form. The composition of the ISM may be related to the relative numbers of carbon- and oxygen-rich stars. For stars with masses less than 8M, the helium burning shell converts more and more of the helium into carbon and then into oxygen, increasing the mass of the carbon-oxygen core. At the same time, the core continues to contract slowly, causing its central density to increase. hence,

electron degeneracy pressure starts dominating. For stars with ZAMS masses less than about 4 M_{\odot} , the carbon–oxygen core will never become large enough and hot enough to ignite nuclear burning. On the other hand, if the important contribution of mass loss is ignored for stars between 4 M_{\odot} and 8 M_{\odot} suggests that the C–O core would reach a sufficiently large mass that it could no longer remain in hydrostatic equilibrium, even with the assistance of pressure from the degenerate electron gas. The outcome of this situation is catastrophic core collapse. The maximum value of 1.4 M_{\odot} for a completely degenerate core is known as the Chandrasekhar limit. Including mass loss, they transition to ONeMg cores, with core masses below the Chandrasekhar limit. The rate of mass loss accelerates with time because the luminosity and radius are increasing while the mass is decreasing during continued evolution up the AGB.

Post AGB With only a very thin layer of material remaining above them, the hydrogen- and helium-burning shells are extinguished, and the luminosity of the star drops rapidly. The hot central object, now revealed, will cool to become a white dwarf star, which is essentially the old red giant’s degenerate C–O core (or ONeMg core in the case of the more massive stars), surrounded by a thin layer of residual hydrogen and helium. These then expel the envelopes into the ISM, resulting in planetary nebulae.

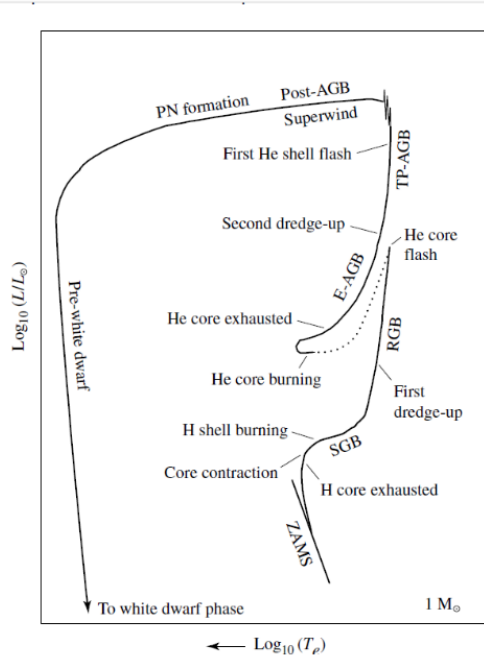


Figure 2: The evolution of a low-mass star of 1 M_{\odot} from the zero-age main sequence to the formation of a white dwarf star. The dotted phase of evolution represents rapid evolution following the helium core flash. The various phases of evolution are labeled as follows: Zero-Age-Main-Sequence (ZAMS), Sub-Giant Branch (SGB), Red Giant Branch (RGB), Early Asymptotic Giant Branch (E-AGB), Thermal Pulse Asymptotic Giant Branch (TP-AGB), Post- Asymptotic Giant Branch (Post-AGB), Planetary Nebula formation (PN formation), and Pre-white dwarf phase leading to white dwarf phase.

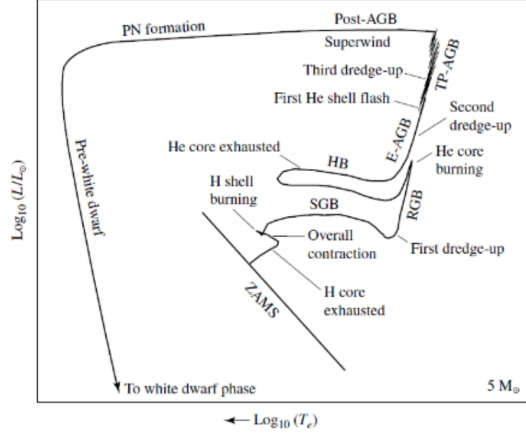


Figure 3: A schematic diagram of the evolution of an intermediate-mass star of $5 M_{\odot}$ from the zero-age main sequence to the formation of a white dwarf star. It is labelled similarly to the above, with an additional Horizontal Branch.

2.2 Dynamical Instability

2.2.1 One-zone model [4]

Consider an unrealistic, yet informative model of stellar pulsation called the one-zone model. According to this model, the star consists of a central point mass equal to the entire mass of the star M , surrounded by a single thin spherical shell of radius R and mass m representing the surface of the star. The interior of the shell is filled with a massless gas of pressure P whose sole function is to support the shell against the gravitational pull of the central mass M . Newton's second law applied

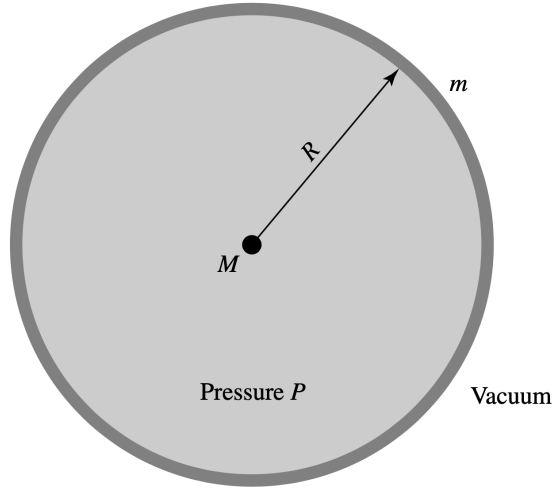


Figure 4: One-zone model of a pulsating star.

to the shell is

$$\rho \frac{d^2 r}{dt^2} = -\frac{GM_r \rho}{r^2} - \frac{dP}{dr} \quad (12)$$

We now linearize radius and pressure, as the amplitude of oscillations is quite small.

$$R = R_0 + \delta R \text{ and } P = P_0 + \delta P$$

where R_0 and P_0 are equilibrium values. Substituting this into the eq. and using first-order approximations, we get

$$m \frac{d^2(\delta R)}{dt^2} = \frac{2GMm}{R_0^3} \delta R + 8\pi R_0 P_0 \delta R + 4\pi R_0^2 \delta P \quad (13)$$

We now assume our model to be adiabatic to get a relation between P and R , which is nothing but

$$PR^{3\gamma} = \text{const.}$$

The linearized version of this expression is

$$\frac{\delta P}{P_0} = -3\gamma \frac{\delta R}{R_0} \quad (14)$$

Using this and the newton's second law for the equilibrium model, we get

$$\frac{d^2(\delta R)}{dt^2} = -(3\gamma - 4) \frac{GM}{R_0^3} \delta R \quad (15)$$

If $\gamma > 4/3$, the equation is that of simple harmonic motion where

$$\omega^2 = (3\gamma - 4) \frac{GM}{R_0^3} \quad (16)$$

with period

$$\Pi = \frac{2\pi}{\sqrt{\frac{4}{3}\pi G \rho_0 (3\gamma - 4)}} \quad (17)$$

where $\rho_0 = M/\frac{4}{3}\pi R_0^3$ is the average density of the equilibrium model.

If $\gamma < 4/3$ we have a dynamically unstable model where $\delta R = Ae^{-\kappa t}$, which means that the increase in gas pressure is not enough to overcome the pull of gravity, resulting in a collapse.

2.2.2 Homologous model

Consider two models of mass M and M' , and radii R and R' . Homologous points are those points in the two models where

$$\frac{r}{R} = \frac{r'}{R'}$$

where r and r' are the radial distances. The two stars are said to be homologous if their homologous mass shells ($m/M = m'/M'$) are situated at homologous points (m is the interior mass at some r). Define the mass coordinate to be $x = m/M$. Then the mass conservation equation becomes

$$\frac{dr}{dx} = \frac{M}{4\pi r^2 \rho}$$

Putting the 's gives the mass conservation equation in the ' star. Substituting $r = r'R/R'$ in the above equation, we get

$$\frac{dr'}{dx} = \frac{M'}{4\pi r'^2 \rho'} \left[\frac{\rho'}{\rho} \frac{M}{M'} \left(\frac{R'}{R} \right)^3 \right]$$

By arguing that the term in square brackets must be 1, we have

$$\frac{\rho'}{\rho} = \frac{M'}{M} \left(\frac{R'}{R} \right)^{-3} = \frac{m'}{m} \left(\frac{r'}{r} \right)^{-3}$$

Now, say we perturb the system homologously by changing the radii of every mass shell by the same factor $r' = r(1+x)$. As m remains constant, we have $\rho' = \rho(1-3x)$. Assuming this change to happen at a very fast timescale, we can take this change to be adiabatic, with a constant adiabatic exponent γ . Putting this into the hydrodynamic equation 12, and proceeding the same way, assuming the changes to be small, making first order approximations and taking the unprimed quantities to satisfy the hydrostatic equilibrium conditions, we get

$$\frac{d^2x}{dt^2} = \frac{GM_r}{r_0^3} (4 - 3\gamma)x$$

The same dynamical instability argument as before follows.

This is a local treatment of dynamical instability. It is very likely that near to the surface $\gamma > 4/3$. But, the surface layers do not contribute much to the stability of the star. Through a more rigorous derivation given in the linked papers ([21] and [22]), we have the following equations of pulsation, at any radial coordinate r

$$\frac{\delta r}{r_0} = \xi e^{i\omega t}$$

where

$$\omega^2 = - \frac{(3\bar{\Gamma} - 4)\Omega_0}{I_0}$$

$$\bar{\Gamma} = \frac{\int_0^R \Gamma P_0 dV_0}{\int_0^R P_0 dV_0}$$

$$\Omega_0 = -3 \int_0^R P_0 dV_0 \quad \text{and} \quad I_0 = \int_0^R r_0^2 dm$$

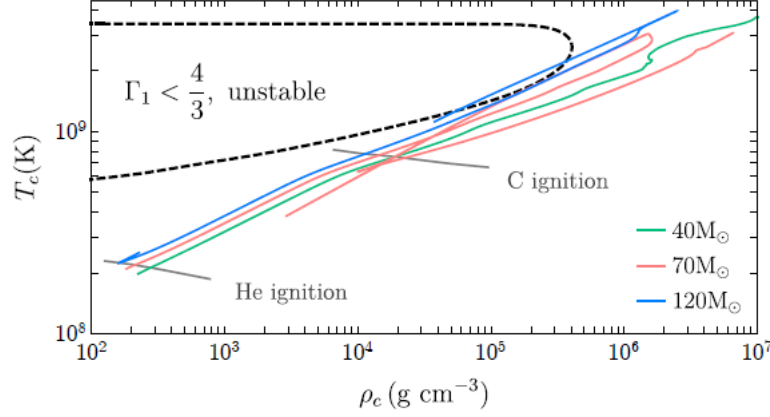
Here the subscript 0 signifies the equilibrium values. The main assumption made here is that ξ is a constant. Through this method it is easy to see that dynamical instability sets in when $\bar{\Gamma} < 4/3$. This pressure weighted value for the EOS ensures that the surface layers do not contribute much, and it's required that $\gamma < 4/3$ over a significant range to contribute to dynamical instability.

2.3 Pair-instability

Pair production is an important endothermic process, which is characterized by -

$$\gamma \longrightarrow e^- + e^+$$

From basic STR, we know that this cannot happen in free space, and there needs to be a recoil of some nuclei nearby to take on the momentum. The threshold photon energy required to produce



H

Figure 5: The evolution of the central density and temperature of population-III stars of initial metallicity $Z_{\odot}/10$ with initial mass $M_{\text{in}} = 40M_{\odot}$, $70M_{\odot}$, and $120M_{\odot}$

these pairs is $E = 2m_e c^2$. Using $E \approx k_B T$, this corresponds to the core temperature of around $10^{10} K$, however this begins to occur at around $8.5 \times 10^8 K$ also. This is possible due to the large number of photons in the star: even though the high-energy tail of the Bose-Einstein distribution is exponentially suppressed by e^{-10} , this still represents a large number of e-p pairs.

If e-p pairs are produced near the threshold, they are almost at rest/have non relativistic velocities. This effectively lowers the EOS $\Gamma = \left(\frac{\partial P}{\partial \rho} \right)_s$, making it closer to the dynamical instability around $4/3$. Essentially, these pairs contribute to the density, but not the pressure close to the threshold, which lessens the pressure holding the gravity in equilibrium, thus destabilizing the star and resulting in contraction. The contraction increases the T of the core, resulting in more e-p pairs, and more instability, causing a further collapse inward. Only when oxygen is explosively ignited, does the star reverse the inward collapse.

We now look at a figure by [7] where they plot the instability region ($\Gamma < 4/3$) in the $T_c - \rho_c$ plane. This is of course not accurate since what we really need to do as described in the Dynamical Instability part is to actually take an integral over the entire star. This can be seen for the $70M_{\odot}$ star, where even though Γ is never less than $4/3$, it does undergo dynamical instability and pulsates. This is because even though the centre of the $70M_{\odot}$ does not evolve into the instability region, the outer layers of the CO core do. We understand the plot as follows -

- In the low T region, the temperatures are too low for sufficient e-p pairs to be formed, which does not affect Γ by a large enough amount to cause an instability.
- The upper edge of the instability region is due to the fact that the e-p pairs now have relativistic velocities (the electron-positron EOS is $\Gamma \approx 4/3$) so they contribute significant pressure to the star and render it stable against gravitational collapse.
- The right hand edge for large densities correspond to the gas pressure of ions and is non negligible. The e-p pairs do not appreciably change the EOS since the stars are mainly supported

by the pressure of ions which are non-relativistic, having EOS $\Gamma \approx 5/3$, making the star stable and unaffected by any e-p production.

2.4 Oxygen ignition

Direct core collapse is the outcome for a star with initial mass (mass of He star at the onset of He burning i.e ZAHB) in the range $25M_{\odot} \lesssim M_{in} \lesssim 50M_{\odot}$ (where the bracketing values are metallicity dependent). Such stars never experience the pair instability discussed above, but instead experience a gravitational instability and collapse directly to a black hole after they establish a sufficiently heavy iron core mass and run out of combustible fuel (see 2.5). This would be the fate of all massive stars if not for the pair instability. The pair instability triggers contraction when the star still has a significant fraction of combustible material. Thus, after the collapse is initiated, and the density is increased throughout the stellar volume, violent fusion reactions can take place, with differing effects depending on the ratio of ^{12}C to ^{16}O .

For the range of initial stellar masses $50M_{\odot} \lesssim M_{in} \lesssim 90M_{\odot}$ ($Z \sim 10^{-3}$) the star will expand again after the initial contraction induces thermonuclear O-burning, in a cycle known as pulsation. Oxygen in the core ignites in the temperature range of $(1.5\text{--}2.6) \times 10^9$ K and in the density range of $(2.6\text{--}6.7) \times 10^{12} \text{ kg}\cdot\text{m}^3$. The principal reactions are given below



The pulsation ejects loosely bound material from the outer volume of the star; this can happen once or multiple times, and the star can lose a small or large fraction of its mass in each pulsation. If the star experiences one or more pulsations but maintains a gravitationally bound core, the star is said to undergo the PPISN (pulsational pair-instability supernova) as the remnant can proceed to core collapse and BH formation. At higher initial mass $90M_{\odot} \lesssim M_{in} \lesssim 240M_{\odot}$ (again for $Z \sim 10^{-3}$), the initial contraction results in such an intense period of explosive oxygen burning that the star unbinds entirely. This explosion with no BH remnant defines the PISN (pair-instability supernova).

2.5 Core Collapse Supernova [4]

The post-main-sequence evolution of stars more massive than $8M_{\odot}$ is decidedly different. Although hydrogen is converted to helium on the main sequence, followed by helium burning leading to a carbon-oxygen core, the very high temperature in the core of a massive star means that carbon and oxygen can burn as well. The end result is that rather than a star ending its life through a planetary nebula, a catastrophic supernova explosion occurs instead. Supernova types Ib, Ic, and II follow the core collapse supernova mechanism.

Following the various nuclear reactions that occur in the core of the star, an “onion-like” shell structure develops in the interior of the star. Following carbon burning, the oxygen in the resulting neon-oxygen core will ignite, producing a new core composition dominated by $^{28}_{14}\text{Si}$. Finally at

temperatures near 3×10^9 K, silicon burning can commence. Silicon burning produces a host of nuclei centered near the ${}^{56}_{26}\text{Fe}$ peak of the binding energy per nucleon curve giving rise to an iron core.

At the very high temperatures now present in the core, the photons possess enough energy to destroy heavy nuclei through a process known as photodisintegration.



This process of stripping down heavier elements to individual protons and neutrons is highly endothermic. Thus, thermal energy is removed from the gas that would otherwise have resulted in the pressure necessary to support the core of the star. Under the extreme conditions that now exist, the free electrons that had assisted in supporting the star through degeneracy pressure are captured by heavy nuclei and by the protons that were produced through photodisintegration.



The amount of energy that escapes a star through neutrinos becomes enormous, far exceeding the photon luminosity.

Through the photodisintegration of iron, combined with electron capture by protons and heavy nuclei, most of the core's support in the form of electron degeneracy pressure is suddenly gone and the core begins to collapse extremely rapidly. In the inner portion of the core, the collapse is homologous, and the velocity of the collapse is proportional to the distance away from the center of the star. At the radius where the velocity exceeds the local sound speed, the collapse can no longer remain homologous and the inner core decouples from the now supersonic outer core, which is left behind and nearly in free-fall.

The homologous collapse of the inner core continues until the density there exceeds $8 \times 10^{17} \text{ kg m}^{-3}$, roughly three times the density of the atomic nucleus. At that point, the nuclear material that now makes up the inner core stiffens because the strong force suddenly becomes repulsive. This is a consequence of Pauli exclusion principle applied to neutrons. The result is that the inner core rebounds somewhat, sending pressure waves outward into the infalling material from the outer core. When the velocity of the pressure waves reach the sound speed, they build into a shock wave that begins to move outward.

As the shock wave encounters the infalling outer iron core, the high temperatures that result cause further photodisintegration, robbing the shock of much of its energy. At this point, the shock stalls, becoming nearly stationary, with infalling material accreting onto it. In other words, the shock has become an accretion shock. However, below the shock, a neutrinosphere develops from the process of photodisintegration and electron capture. Since the overlying material is now so dense that even neutrinos cannot escape, some of the neutrino energy (5%) will be deposited in the matter just behind the shock. This additional energy heats the material and allows the shock to resume its march to the surface. If this does not happen quickly enough, the initial outflowing material will fall back onto the core, meaning that an explosion doesn't occur. Assuming that the shock is able to resume its march towards the surface, the shock will drive the envelope and the remainder of the nuclear-processed matter in front of it.

If the initial mass of the star on the main sequence is not too large ($M_{\text{ZAMS}} < 25M_{\odot}$), the remnant

in the inner core will stabilize and become a neutron star, supported by neutron degeneracy pressure. However, if the initial stellar mass is much larger, even the pressure of neutron degeneracy cannot support the remnant against the pull of gravity, and the final collapse will be complete producing a black hole (an object whose mass has collapsed to a singularity of infinite density).

2.6 How Massive Single Stars End their Life [15]

In this section, we attempt to trace the histories of massive stars and give a description of the fate of stars of different masses and metallicities. We will also describe the various supernovae these stars undergo.

2.6.1 Remnant properties

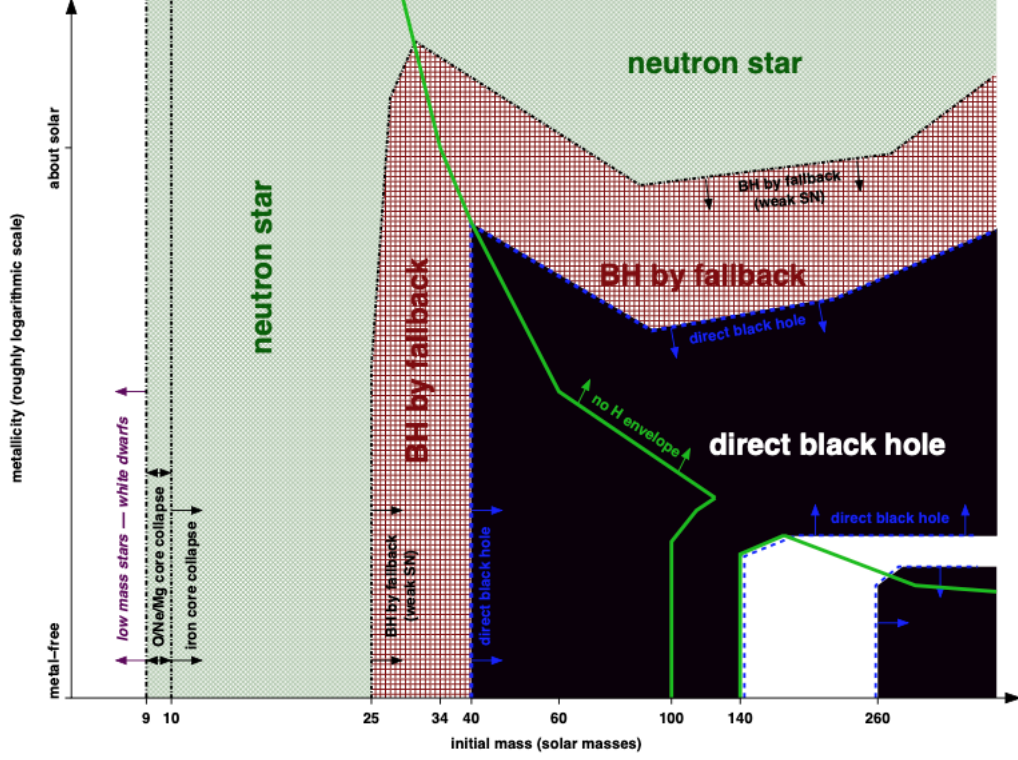


Figure 6: Remnants of massive stars as a function of initial metallicity and initial mass (ZAMS). The thick green line separates the regimes where the stars keep their hydrogen envelope (left and lower right) from those that do not. The dashed blue line indicates the border of the regime of direct black hole formation (black). This domain is interrupted by a strip of pair-instability supernovae that leave no remnant (white). Outside the direct black hole regime, at lower mass and higher metallicity, follows the regime of BH formation by fallback (red cross hatching and bordered by a black dash-dotted line). Outside of this, green cross hatching indicates the formation of neutron stars. The lowest-mass neutron stars may be made by O/Ne/Mg core collapse instead of iron core collapse (vertical dash-dotted lines at the left). At even lower mass, the cores do not collapse and only white dwarfs are made (white strip at the very left) [15]

The principal physics connecting the final evolution of a star to its metallicity is its mass loss. Low metallicity stars have less mass loss and have bigger helium cores and hydrogen envelopes when they die. Fig. 6 shows the remnant types as a function of mass and initial metallicity.

Stars below $\sim 9M_{\odot}$ do not form massive enough cores to encounter iron core collapse. They just end their lives as white dwarfs with their CO core supported through electron degeneracy pressure. Just above this mass lies a narrow range of $\sim 9 - 10M_{\odot}$, where degenerate oxygen-neon cores are formed that either collapse due to electron capture (as there is loss of electron degeneracy pressure)

to form neutron stars or lose their envelopes and make white dwarfs. Above $\sim 10M_{\odot}$, core collapse is the only alternative.

The transition between white dwarf formation and iron core collapse depends very little on metallicity as this boundary is well defined through statistical mechanics. Hence, this appears as a vertical line in Fig. 6. At low metallicities, the boundaries for black hole formation are also defined entirely by the initial stellar mass since there is a one to one correspondence between initial stellar mass and final helium core mass. For stars of higher metallicity, mass loss becomes increasingly important resulting in smaller helium cores for a given initial mass. If the star loses its entire hydrogen envelope, its rate of mass loss increases significantly producing much smaller helium cores at collapse. This explains the abrupt change in the otherwise vertical boundaries between neutron stars, fallback black holes, and direct black holes.

During the course of events that occur in a core collapse supernova (section 2.5), suppose we get a shock after the rebound on the stiffened neutron degenerate core, and the shock stalls which causes some layers to fall back onto the “proto-neutron star”, we get a black hole by fallback. This happens because the layers that fall back onto the proto-neutron star can drive the mass over the threshold mass for neutron stars. For low metallicity stars, black holes by fall back occur for $\sim 25 - 40M_{\odot}$. Above $40M_{\odot}$, low metallicity stars form black holes directly (no supernova shock is launched), while at higher metallicities black holes of smaller masses are produced by fall back until, ultimately, only neutron stars are made. Winds are assumed to be stronger in higher mass stars, so the metallicity at which these transitions occur decreases with mass.

At low metallicities, there is also a range of masses for massive stars that leave behind no remnant whatsoever. These are the pair-instability supernovae which are explained in detail in section 3.

3 The Black Hole Mass gap

In section 2.4, we saw that stars in the initial mass range $50M_{\odot} \lesssim M_{in} \lesssim 90M_{\odot}$ undergo PPISNe leaving behind black hole remnants, and stars in the mass range $90M_{\odot} \lesssim M_{in} \lesssim 240M_{\odot}$ undergo PISNe leaving behind no remnants. For higher initial masses $M_{in} \gtrsim 240M_{\odot}$ ($Z = 10^{-3}$), the freely falling stellar material, after the onset of pair-instability, heats up to such a degree on the inward journey that the nuclei photodisintegrate. This means that PISN is prevented as there is not enough energy for pulses. The star continues to evolve until Fe core collapse (See image 7).

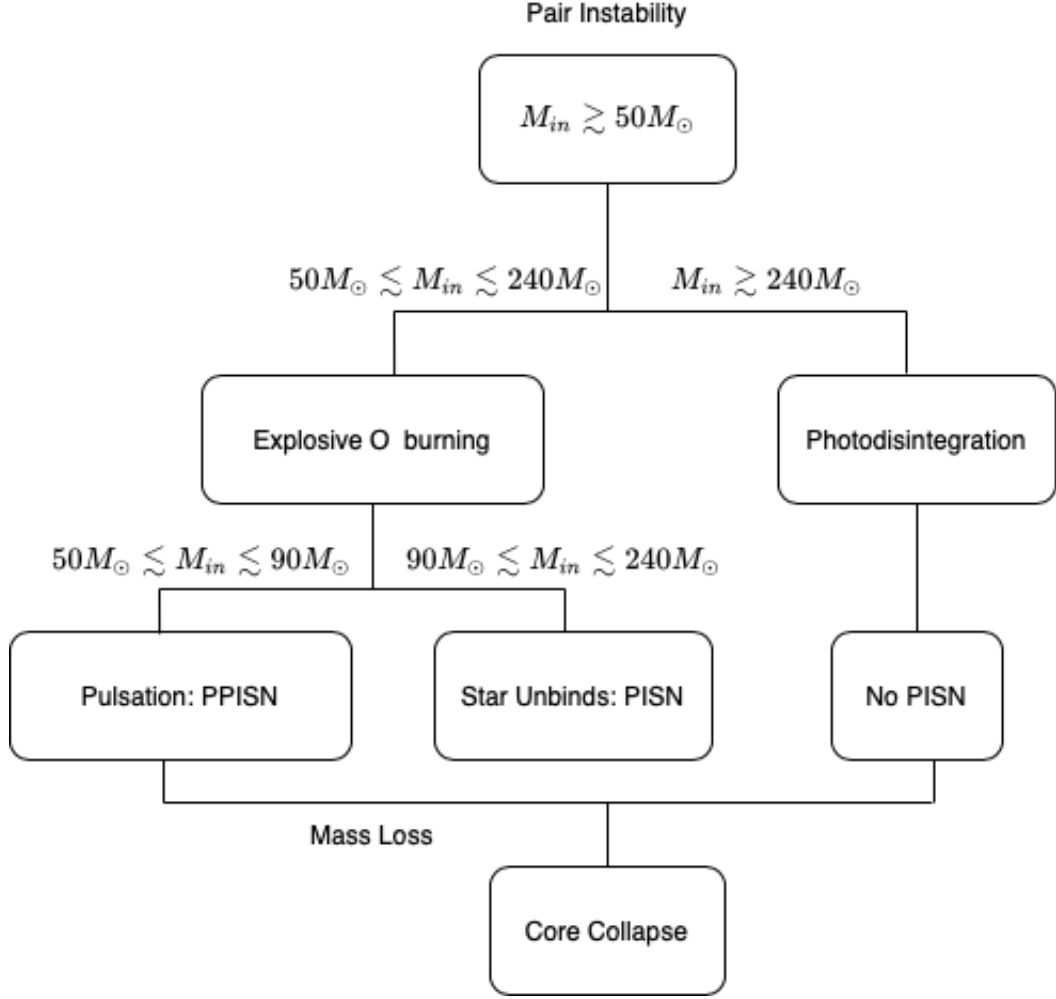


Figure 7: Flowchart describing the various processes at different masses

The occurrence of these PISNe is what results in a mass gap as no BH remnant is left behind. However, the lower edge of the mass gap is set by the mass lost during pulsations in a PPISN. As we increase star mass, initially we see an increase in the final black hole mass as expected. Eventually, additional mass loss is encountered due to pair-instability pulsations. Thus, the greatest black hole mass, which forms the lower edge of the mass gap, is set by a massive enough star which at the same time isn't that massive that it loses significant amount of mass due to pulsations. We can see this in figure 8. The upper edge of the mass gap turns out to be $\sim 130M_{\odot}$ - the lightest BH to be formed out of a star that escapes PISNe due to photodisintegration.

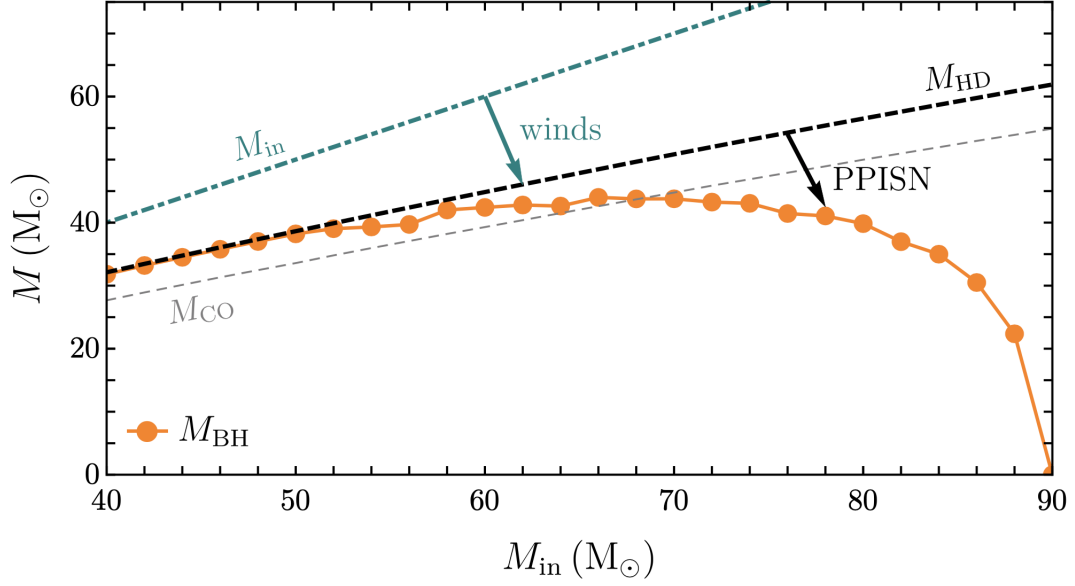


Figure 8: Various masses as a function of initial stellar mass M_{in} (mass at ZAHB) for Pop. III stars of metallicity $Z_{\odot}/10$. The teal dot-dashed line shows the initial mass, the black dashed line shows the entire mass of the star at helium depletion, and the dashed gray line shows the CO core mass at helium depletion. The orange points correspond to final black hole mass. The PPISN occurs at higher masses, leaving no compact object in the final state [7].

3.1 Known Physics Dependence of the BHMG [10]

3.1.1 Metallicity

Recall metallicity is the abundance of elements present in an object that are heavier than hydrogen and helium. We vary the metallicity ranging from 10^{-5} to 3×10^{-3} . Metallicity primarily affects the evolution of a helium core by varying the amount of mass-lost via winds. $dM/dt = Z^{0.8}$ is derived for wind mass loss, mainly occurring during helium burning (empirically for O and B stars in [25]). Hence lower values of Z results in heavier BH due to less mass loss and at very high Z , stars lose sufficient mass so as to not enter the PI region, and simply undergo core collapse. Fiducial metallicity is taken as 10^{-3} in [10].

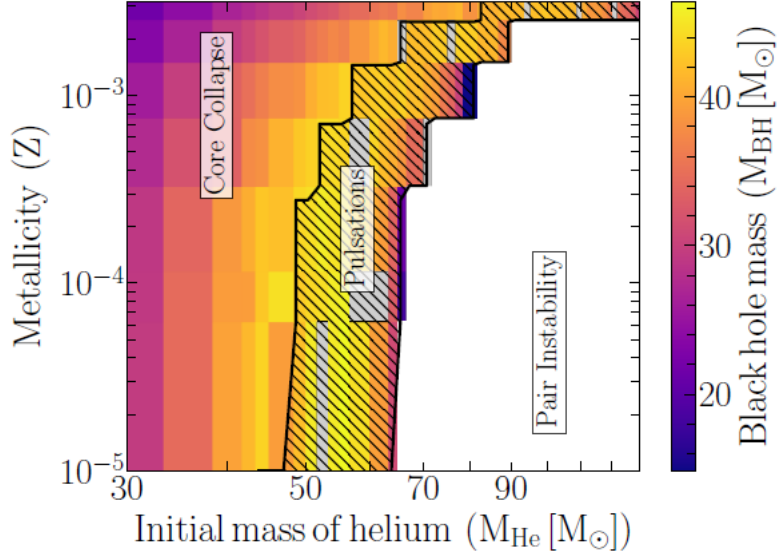


Figure 9: The mass of the BH formed as function of the metallicity of the star and its initial helium star mass.

In figure 9, let's traverse the x axis. At first, as the He core mass increases, so does the resulting BH mass due to the larger initial mass of the star. However, once the star enters the pulsational regime, it begins to lose mass. As the core mass increases, the pulses decrease in number (Low mass stars have weak pulses owing to the low amount of O in the core. These weak pulses drive out less mass, hence star returns to an almost similar state as before. Thus, the star needs to have multiple pulses to drive out sufficient mass to regain stability) but become more energetic (due to larger O in core now), driving out more mass in each pulse. Increasing the mass further, the first pulse itself disrupts the entire star in a PISN.

On the y axis, as the initial metallicity of the star increases, the mass of the BH decreases for fixed initial helium core mass. This is due to an increase in the amount of mass lost via winds before the star enters the PPI region, which decreases the final mass of the star before collapse.

We now study the tighter relation of BH mass as a function of the CO core mass (at helium depletion) over our metallicity range.

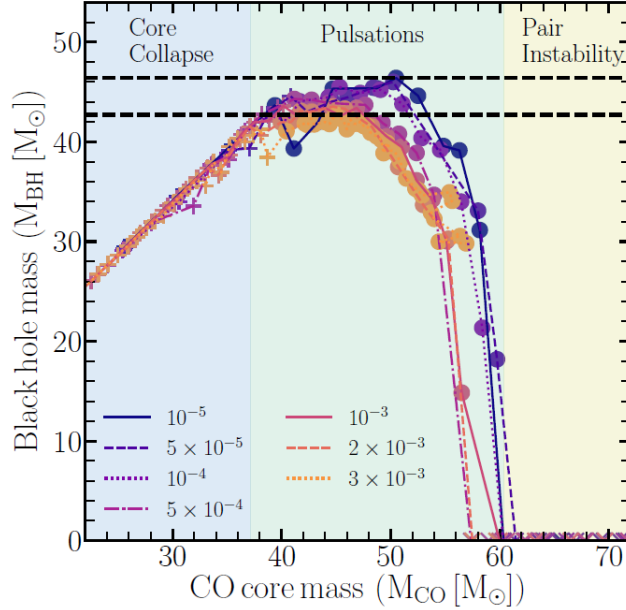


Figure 10: Mass of final BH as a function of the CO core mass, for different metallicities. Circles denote models that underwent at least one pulse, pluses evolved directly to CC, and crosses underwent a PISN

The upper edge of the PPISN region slightly decreases as the metallicity increases. The most massive BHs do not come from those with the most massive CO cores that undergo a PPI, due to the pulses becoming stronger and thus driving more mass loss, but come from somewhere in the middle. The models of the paper span over 2.5 orders of magnitudes in metallicity, but over such a wide range the maximum BH mass decreased only by $3M_{\odot}$. In the following sections, a fiducial metallicity of 10^{-3} is used.

3.1.2 Wind Mass Loss

Mass loss via winds is not self-consistently solved in 1D stellar evolution models since they require the solutions to 3D hydrodynamical equations, but instead, is set by a mass loss prescription and that functional form can have a large impact on the star’s evolution. The authors of [10] investigate using the H, N&L and T algorithms, along with no mass loss also. They also use a clumpiness factor η which is related to the inhomogeneities in winds, given by $\eta = \langle \rho^2 \rangle / \langle \rho \rangle^2$, where ρ is the wind mass density, and average is taken spatially. η is varied between 0.1 and 1.

As the strength of mass loss increases, by changing the wind loss prescription, the CO-BH mass distribution flattens and decreases the maximum BH mass. Overall, in the values of η considered, the total mass loss change is of $4M_{\odot}$. For the H algorithm, increasing η to 1, increases mass loss to an extent that no model enters pulsation region.

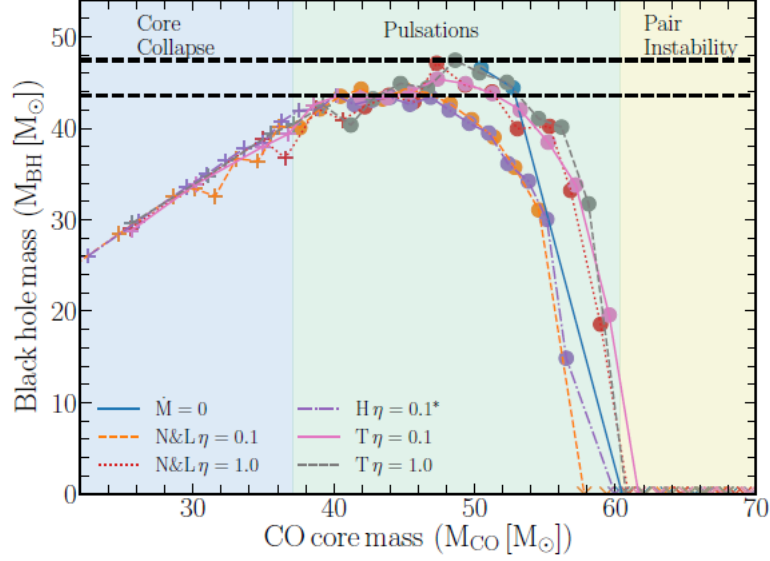


Figure 11: Fig shows variations in the wind mass loss prescription; H, N&L and T while η varies between 0.1 and 1.0. Colour shading shows the regions between the CC, PPISN, and PISN outcomes for our fiducial set of physics assumptions.

3.2 Nuclear Physics

Varying nuclear reaction rate within its known uncertainties has been shown to have a large impact on the stellar structure of a star, since the rates are very sensitive to temperature. MESA by default uses the NACRE and REACLIB libraries, whereas the authors of [10] use STARLIB, and vary reaction rates with $\pm\sigma$ uncertainty. They test variations in three rates;

- 3α (triple alpha reaction) : $3\alpha \longrightarrow {}^{12}\text{C} + 2\gamma$
- $C12\alpha$ reaction : $\alpha + {}^{12}\text{C} \longrightarrow {}^{16}\text{O} + \gamma$
- $O16\alpha$ reaction : $\alpha + {}^{16}\text{O} \longrightarrow {}^{20}\text{Ne} + \gamma$

They also use different nuclear networks to see the impact on the stars, using *approx21.net*, *mesa75.net* and *mesa128.net*.

They observe that $O16\alpha$ has minimal effects on the BHMG. Varying either 3α or $C12\alpha$ has large impacts on the BHMG. As the $C12\alpha$ rate decreases, lesser O is produced, and a less violent explosion occurs, increasing max BH mass. Within the 1σ interval for the $C12\alpha$, the maximum BH mass varies by $18M_{\odot}$. This is the most significant variation, leading to a 40% variation in max BH mass.

As the 3α rate increases, the maximum BH also increases since the mass fraction of C in core increases, which represses explosive burning of O. This causes a variation of over $8M_{\odot}$ within the 1σ interval for the 3α . Higher carbon fractions also decrease the range in CO core mass within which models undergo pulsations, decreases the number of models undergoing strong pulsations, weakens the pulses to not eject large amounts of mass, and also sharpens the BH mass distribution.

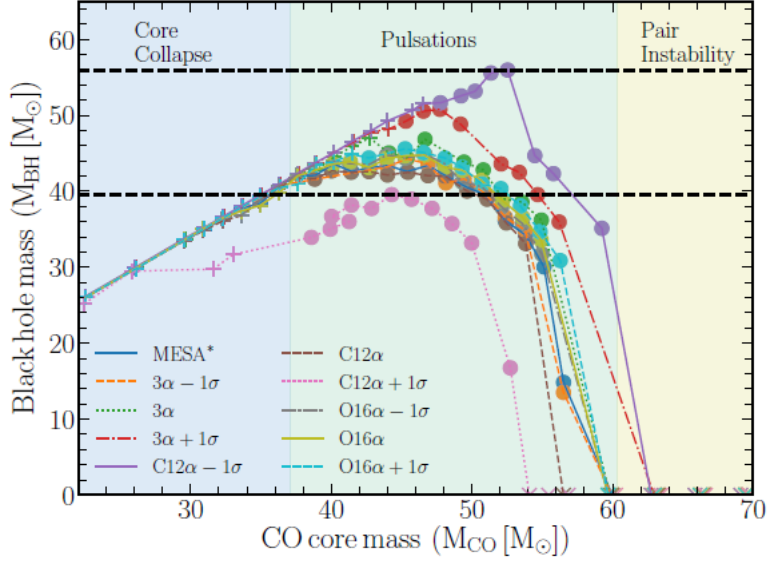


Figure 12: Fig shows BH mass as a function of CO core mass with the variations in the reaction rates as given using STARLIB, and the green MESA graph as the one from default MESA rates

3.3 Neutrino losses

With higher core temperatures and densities the rate of thermal neutrino losses increases. The stronger the cooling, the more energy is required from nuclear burning to overcome these losses. As neutrino losses dominate only after He depletion and during carbon burning, an increase in the CO reaction rate would result in more oxygen present when pair-instability sets in. This would lead to stronger pulses, decreasing the final black hole mass.

The main neutrino losses are due to -

- Pair annihilation - dominant in massive stars, and after helium depletion

$$e^+ + e^- \longrightarrow \nu_e + \bar{\nu}_e$$
- Photoneutrino processes - Analogue of Compton scattering with the outgoing photon replaced by a neutrino pair. Significant during helium and carbon burning

$$\gamma + e^- \longrightarrow e^- + \nu + \bar{\nu}$$
- Plasma neutrino process - Important at high densities where the plasma frequency is high and ω plasma can be comparable to kT . That is, in white dwarfs and evolved cores of massive stars. Plasmons are collective charge oscillations in plasma, coulomb force as restoring forces, behaves as a photon with rest mass (acquires mass by propagating through plasma)

$$\gamma_{plasmon} \longrightarrow e^- + e^+ \longrightarrow \nu + \bar{\nu}.$$
- Bremsstrahlung (electron nucleus)- Electron screening can modify coulomb interaction, important when electrons are strongly degenerate, and in neutron stars

$$(Z, A) + e^- \longrightarrow (Z, A) + e^- + \nu_e + \bar{\nu}_e.$$

- Recombination - Neutrino pair emission due to capture of a free electron into the K-shell of a fully ionized atom

$$e_{\text{continuum}}^- \longrightarrow e_{\text{bound}}^- + \nu_e + \bar{\nu}_e.$$

They also vary the Weinberg angle, which determines the rate of neutrino loss. Increasing Weinberg angle increases neutrino cooling rate. Over the whole range, neutrino rates vary upto 3%.

The overall effect is very small, maximum variation being $1M_\odot$. As the rate increases, a less massive BH formed. As Weinberg angle varies, a variation of $1.5M_\odot$ is observed. Smaller Weinberg angle (leading to smaller coupling, hence more neutrinos) results in lower maximum BH mass.

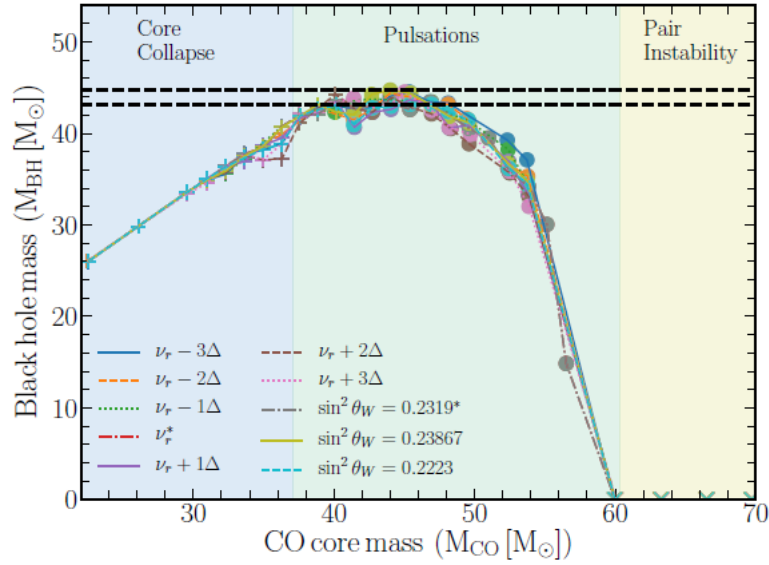


Figure 13: Variations in BH mass as function of CO core mass due to the numerical uncertainties in the fits, and the Weinberg angle

3.3.1 Convective mixing

The authors test uncertainties in convective mixing within the framework of mixing length theory (MLT), and vary MLT's α_{MLT} efficiency parameter between 1.5 and 2.0 with 2.0 being the default value (see section 2.1.3). At the convective boundaries, they assume convective overshoot mixing occurs with an exponential profile. Overshoot is basically a phenomenon where convection carries material beyond the unstable region (convective region) into a stable region due to the momentum of the convecting material. This phenomenon in MLT is parameterized into two terms- f_{ov} and f_0 . The first term dictates the scale height of the convective overshoot in units of pressure scale height. The second term dictates the starting point inside the convective boundary from where the overshoot begins, in pressure scale heights. f_{ov} was varied between 0 and 0.05, with $f_{ov} = 0.01$ being the default. f_0 was set to 0.005

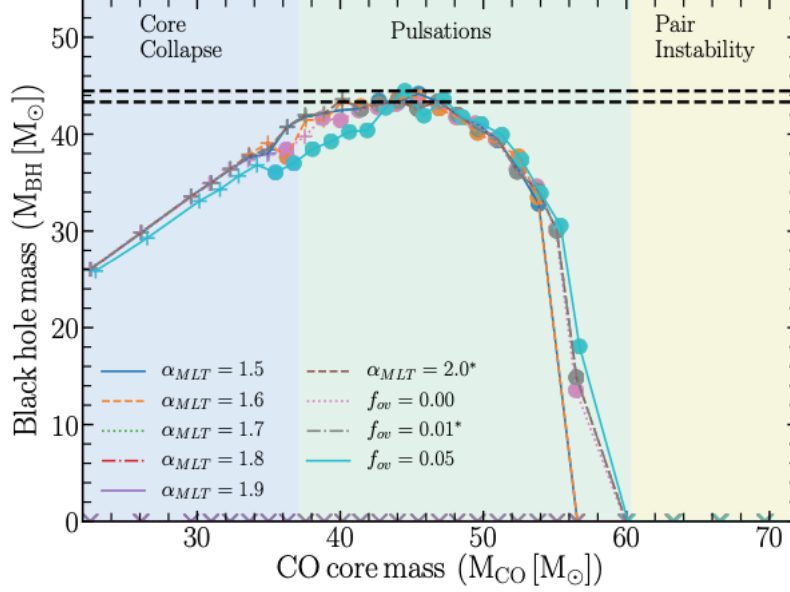


Figure 14: Final BH masses as a function of CO core mass for different values of α_{MLT} f_{ov} .

Simulations using MESA showed that there is very little change in the BH masses as α_{MLT} is varied, with the BH masses slightly decreasing as α_{MLT} increased. The effect of varying f_{ov} was also found to be quite small. But, a significant difference occurred at the PPISN/CC boundary where $f_{ov} = 0.05$, decreased the final BH mass relative to the lower f_{ov} models. This can be understood as follows. When f_{ov} is small, the star has a separate off-center and a central burning region, both of which drive convections. When f_{ov} increases, the convection zones can merge, which increases the available fuel supply and causes the pulses to become stronger, driving increased mass loss.

3.4 Effect of novel particle emissions

Here, the authors of [7] claim that the emission of Beyond Standard Model particles changes stellar dynamics. The main BSM particles they consider are -

Electrophilic Axions (ae) : These are Axions coupling to electrons, with $\alpha_{26} = 10^{26} g_{ae}^2 / 4\pi$, where g is the dimensionless coupling. In the ranges of interest, the axions are massless and electrons are non relativistic and non degenerate, and we use α_{26} of order of 0-2. The main energy losses due to these axions are by the -

- Semi Compton scattering - $\gamma + e \longrightarrow e + a$ (dominates specific energy loss rate during helium burning), with energy loss prop to T^6 and the coupling
- Bremsstrahlung energy loss - $e + (Z, A) \longrightarrow e + (Z, A) + a$, dominates energy loss rate at higher densities, and is prop to coupling, ρ and $T^{2.5}$ in non degenerate and T^4 in degenerate.

Photophilic axions (a γ) These are axions interacting with photons, with coupling $g_{10} = g_{a\gamma} / 10^{10}$ GeV, where $g_{a\gamma}$ is the dimensionful coupling. Energy loss rate is due to -

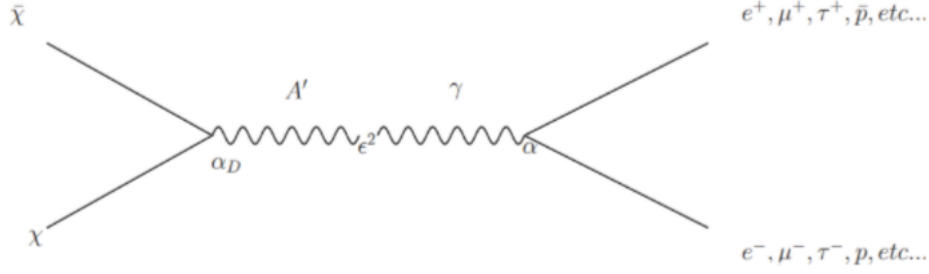


Figure 15: Fig: Shows χ (WIMP) coupling with a hidden photon

- Primakoff process (production of axions by light and nuclei) given as $\gamma + e, I \longrightarrow e, I + a$, with the loss rate prop to $g_{a\gamma}^2 T^7 \rho^{-1}$. Emission is screened at high temp and low density

Hidden Photons (A') These kinetically mix with SM photons (ϵ is kinetic mixing factor), and couple with charged particles. Hidden photons with $m_{A'} < w$ (plasma mass), are screened. Specific energy loss rate depends on longitudinal modes of hidden photons, T and $\epsilon^2 m_A^2$. A density dependence arises only when plasma mass experiences Boltzmann suppression.

3.4.1 General Effects

To understand the effects of new particle losses on the black hole mass gap, we first see how these losses effect individual stars. As more energy is needed to compensate for increased losses and provide the requisite pressure necessary to maintain hydrostatic equilibrium, the primary effect of new particle losses is to reduce the lifetime of nuclear burning as the supply of nuclear fuel is finite. Thus, the time for a ZAHB star to reach helium depletion is reduced. There are two important consequences of this reduced helium burning lifetime:

- As winds are usually active during helium burning, the mass lost due to winds is decreased.
- As the reaction $^{12}\text{C}(\alpha, \gamma)^{16}\text{O}$ occurs in conjunction with the triple alpha process during helium burning, the ratio of ^{12}C to ^{16}O is increased at helium depletion.

As we saw in section 2.4, oxygen is the fuel for PPISN. An increase in the amount of carbon at the onset of pair instability would suppress oxygen burning, resulting in weaker pulses and less mass lost due to pulses. Combined with the effect of less mass lost due to winds, the observable consequences of novel energy losses is that stars collapse to form heavier black holes. Of the two effects, suppression of PPISN seems to be a far more important effect.

3.4.2 Energy Loss Contours

We now see the impact of temperature dependence on the energy loss rates of the electrophilic axion, photophilic axion, and hidden photon in the plot of contours of constant loss rate in Fig. 16. The blue track shows the evolution of a star of initial mass $M_{in} = 55M_{\odot}$ ($Z = 10^{-5}$ with no new particle emission) from ZAHB to the onset of carbon ignition. The presence of the orange dotted line, which signifies the point where neutrino losses dominate, well beyond the point of helium depletion validates the argument for assessing the impact of novel losses based on shortening the time to

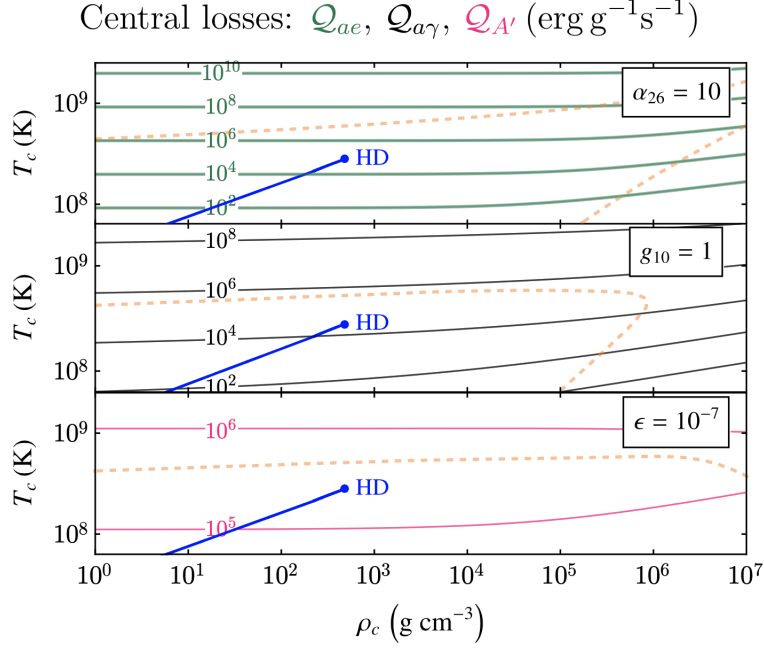


Figure 16: Contours of rate of specific energy loss due to electrophilic axions, photophilic axions, and hidden photons with $Z/A = 1/2$ in the $T_c - \rho_c$ plane, with a sample track of $M_{in} = 55M_\odot$, $Z = 10^{-5}$ star followed until core helium depletion (HD). The dashed orange line denotes when neutrino losses dominate.

helium depletion. If neutrino losses dominated well before this time, then adding a new mechanism would not significantly impact the stellar evolution.

The figure also shows the difference in the temperature scaling of the novel particle losses. At low densities, the loss rates scale as

$$\mathcal{Q}_{ae} \propto T^6 \quad (26)$$

$$\mathcal{Q}_{a\gamma} \propto T^4 \quad (27)$$

$$\mathcal{Q}_{A'} \propto T^1 \quad (28)$$

The significance of this difference in scaling is that if we increase the loss rates by increasing the couplings of the new particles, we find that we increase the time-integrated loss due to the hidden photon by more than the corresponding increase in the axion case.

3.4.3 MESA results from [7]

For $Z = 10^{-5}$,

- **Electrophilic axions:** Lower edge shifts from $47M_\odot$ for $\alpha_{26} = 0$ to $56M_\odot$ for $\alpha_{26} = 100$. The upper edge too moves to higher masses by $\sim 8M_\odot$. The shift in upper edge is also due to less mass lost due to winds.

- **Photophilic axions:** Similar effects for photophilic axion as both lower and upper edge shift upwards by a few solar masses at increased g_{10} .
- **Hidden Photons:** Effects of losses more pronounced than the other two cases. This is because of higher time integrated loss, as discussed before, which results in a steeper and tighter correlation with increasing coupling. The lower edge is shifted to as high as $72M_{\odot}$ for high ϵ . The upper edge too shifts by a few solar masses.

An interesting thing to note here is that PPISN is completely quenched in the case of hidden photon coupling constant $\epsilon = 5 \times 10^{-7}$, so the final black hole mass for those stars is approximately equal to the star's mass at helium depletion. This means that the only effects of mass loss are due to stellar winds and, at higher masses, the PISN.

3.4.4 Massive novel particle production

A new particle that is sufficiently massive will not escape from the star's gravitational potential well but will remain inside the core. In this case, the particle will not act as a loss source but will instead contribute to the EOS, provided the coupling to the Standard Model is strong enough to maintain thermal equilibrium. As the instability region is governed by the EOS of all the particles present, production of new particles in the core gives rise to the possibility of new instabilities.

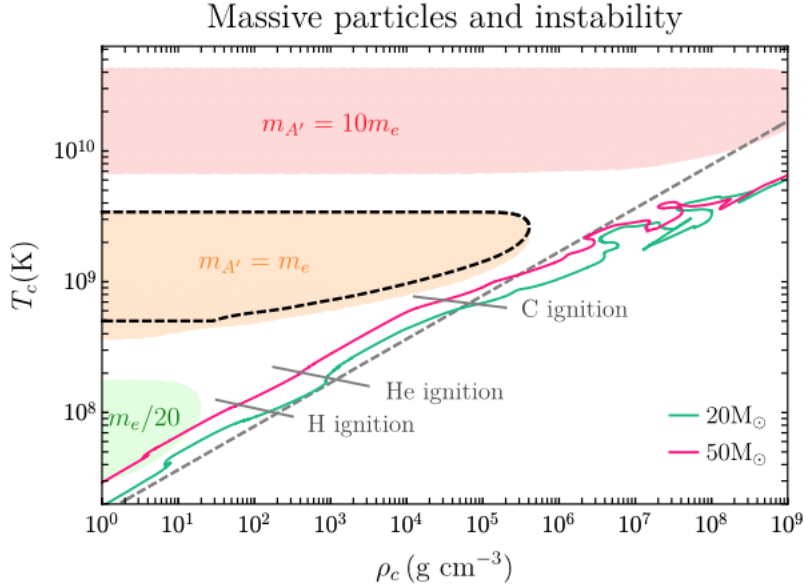


Figure 17: The region in the $T_c - \rho_c$ where $\Gamma_1 < 4/3$ due to the production of new particles X of mass m_X and degeneracy $g_X = 3$. The tracks correspond to stars with metallicity $Z = Z_{\odot}/10 = 0.00142$ evolving from ZAMS. The grey dashed line indicates where the radiation pressure is equal to the gas pressure, with gas pressure dominating at higher densities. The black dashed line indicates the region where e^+e^- pair instability is active.

The authors of [7] consider the equation of state for a gas of ions, radiation, electrons (and positrons), and novel particles X in thermal equilibrium. From Fig. 17, one can see that the tracks do not encounter the instability region for $m_X > m_e$. But, for $m_X < m_e$ it is possible for stars as light as $40M_\odot$ to pass through an unstable region during hydrogen and helium burning. This may result in a thermonuclear explosion as is the case with pair-instability. It is also possible that some stable cycle is reached and the ultimate result is a new type of pulsating or variable star.

4 MESA implementation (overview of MESA)[28]

HLLC (Harten-Lax-van Leer-Contact) solver is a Riemann solver used in MESA to evolve stars mainly through the hydrodynamics stage of evolution. This is required to accurately model shocks and pulses. The stellar structure equations (which are also described below) that MESA solves to obtain equilibrium models is largely the same even during the hydrostatic stage. The main difference is that cell velocities are set to zero and are only turned on when hydrodynamics is active. The conditions that govern when hydrodynamics is turned on and off depends on the specific use case. The controls that specify this in the PPISN test suite of MESA are described in section 6.

4.1 Implementation of HLLC

MESA evolves 1D models consisting of cells that have particular attributes such as radius, mass etc. which do not contain any information of polar and azimuthal angles, which would imply radial symmetry. Even during hydrodynamics, radial symmetry is assumed. We now see the details of the model MESA builds and evolves.

MESA evolves a dynamic mesh, with each cell having a cell-centered velocity u . They are indexed with higher index numbers towards the centre, with cell face radius r_k , with mass contained in cell dm_k , and face area $\mathcal{A}_k = 4\pi r_k^2$, and all thermodynamic variables are defined at cell centres by mass as shown.

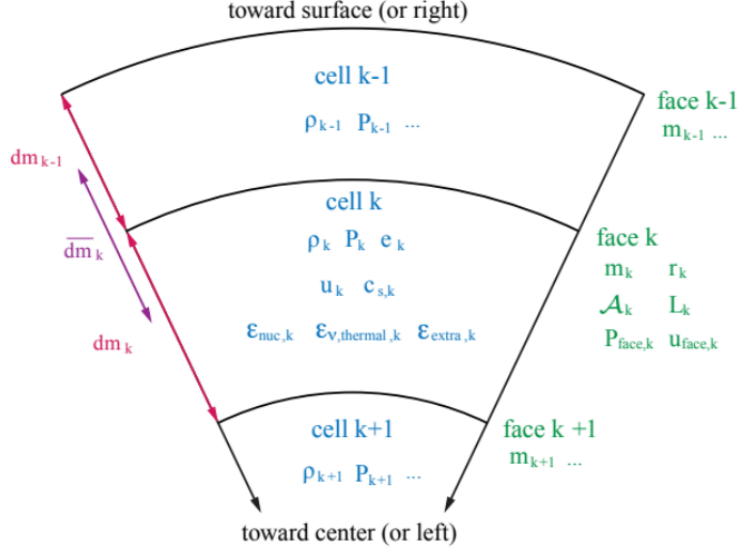


Figure 18: Cell and face variables relevant for hydrodynamics in MESA when using HLLC

We define the densities at the face to be that of the centre of the cell above, ie - $\rho_L = \rho_k, \rho_R = \rho_{k-1}$. The pressure derivative according to hydrostatic equilibrium is

$$\left(\frac{dP}{dm}\right)_{hse} = -\frac{Gm_k}{\mathcal{A}_k r_k^2} \quad (29)$$

we then set

$$P_L = P_k + \frac{dm_k}{2} \left(\frac{dP}{dm}\right)_{hse} \quad (30)$$

and

$$P_R = P_{k-1} + \frac{dm_{k-1}}{2} \left(\frac{dP}{dm}\right)_{hse} \quad (31)$$

Note that we take no mass flux across cell faces.

The contact wave speed is

$$u_{face} = S_* = \frac{u_R \rho_R (S_R - u_R) + u_L \rho_L (S_L - u_L) + P_L - P_R}{\rho_R (S_R - u_R) + \rho_L (S_L - u_L)} \quad (32)$$

with

$$P_{face} = P_* = \frac{1}{2}(\rho_R(u_R - S_R)(u_R - S_*) + P_R + \rho_R(u_L - S_L)(u_L - S_*) + P_L) \quad (33)$$

where S_L and S_R are the fastest wavespeeds towards left and right, with

$$S_L = \min(u_L - c_{s,L}, u_R - c_{s,R}) \quad (34)$$

and

$$S_R = \max(u_L + c_{s,L}, u_R + c_{s,R}) \quad (35)$$

where $c_{s,L}$ is the sound speed on the left of the cell boundary.

The cell boundaries move such that the net fluxes for mass, momentum, and energy from cell k to $k-1$ are $F_{\rho,k} = 0$, $F_{p,k} = \mathcal{A}_k P_{face,k}$, $F_{e,k} = \mathcal{A}_k P_{face,k} u_{face,k} + L_k$, (the latter is due to the convective or radiative transport of energy).

- The mass conservation equation is written as-

$$\ln[r_k] = \frac{1}{3} \ln \left[r_{k+1}^3 + \frac{3dm_k}{4\pi\rho_k} \right] \quad (36)$$

- The equation for radius is

$$r_k = r_{start,k} + u_{face,k} \delta t \quad (37)$$

- The radial momentum equation is (gravitational, its own source term and momentum flux respectively)

$$\frac{u_k - u_{start,k}}{\delta t} = -\frac{1}{2} \left(\frac{Gm_k}{r_k^2} + \frac{Gm_{k+1}}{r_{k+1}^2} \right) + \frac{P_k(\mathcal{A}_k - \mathcal{A}_{k+1})}{dm_k} + \frac{F_{p,k+1} - F_{p,k}}{dm_k} \quad (38)$$

- The energy conservation equation is

$$\begin{aligned} e_k - e_{start,k} + \frac{1}{2}(u_k^2 - u_{start,k}^2) - Gm_C \left(\frac{1}{r_C} - \frac{1}{r_{C,start}} \right) \\ = \delta t \left[\frac{F_{e,k+1} - F_{e,k}}{dm_k} + e_{nuc,k} - e_{v,k} + e_{extra,k} \right] \end{aligned}$$

Here m_C, r_C are the total mass and radius till the face of k . The terms on the left split the local total energy into internal, kinetic, and potential components. The right side gives the energy loss or injection in terms of the fluxes, the nuclear burning term, the neutrino energy loss rate, and other processes.

- The temperature differences of interior cells T_k are set by energy transport across boundaries

$$T_{k-1} - T_k = dm_k \left[\nabla_{T,k} \left(\frac{dP}{dm} \right) \frac{T_k}{P_k} \right] \quad (39)$$

4.2 Energy Accounting in MESA

4.2.1 Fundamental equations

Energy conservation is typically formulated by considering the energy flow in and out of a fluid parcel. Here we use the Lagrangian picture to formulate this (hydrostatic):

$$\frac{Dq}{Dt} = \epsilon - \frac{\partial L}{\partial m} \quad (40)$$

Here, $D/Dt = \partial/\partial t + u\partial/\partial r$ is the Lagrangian time derivative, Dq/Dt is the specific heating rate, ϵ is the specific rate of energy injection into the parcel, and $\partial L/\partial m$ is the specific rate of energy flow through the boundaries; with $L(m)$ being the luminosity profile and m the Lagrangian

mass coordinate. By tradition, the negative of the left- hand side of the above equation is called ϵ_{grav} .

In the entropic representation we have the following thermodynamic relation:

$$dE + PdV = TdS + \sum_i \mu_i dN_i \quad (41)$$

where E is the internal energy, P the pressure, V is the volume, S the entropy, T the temperature, and μ_i the chemical potential of the i th species. This equation is re-written in the specific (per unit mass) form as

$$\delta q = de + Pd\left(\frac{1}{\rho}\right) = Tds + \sum_i \left(\frac{\partial e}{\partial Y_i}\right)_{s,\rho} dY_i \quad (42)$$

where $Y_i \equiv N_i/N_B$ (N_i is the number of atoms of the species and N_B is the total number of Baryons), ρ is the total baryonic mass density, $1/\rho$ is the specific volume, and e and s are the specific energy and entropy respectively.

4.2.2 Implementation in MESA

MESA solves the stellar structure equations implicitly, thus it is possible to approximate total time derivatives of any quantity calculated in the stellar model simply by differencing its value at the start and end of a timestep. Therefore, one way to evaluate ϵ_{grav} would be to directly calculate the time derivatives in Equation 42. Thus a possible expression for ϵ_{grav} could be

$$-\epsilon_{grav} = \frac{De}{Dt} + P \frac{D}{Dt} \left(\frac{1}{\rho}\right) \quad (43)$$

This expression can be written in the following form to improve numerical stability. MESA solves this equation by default.

$$-\epsilon_{grav} = c_P T \left[(1 - \nabla_{ad} \chi_T) \frac{D \ln T}{Dt} - \nabla_{ad} \chi_\rho \frac{D \ln \rho}{Dt} \right] \quad (44)$$

where $c_P \equiv (\partial q / \partial T)_P$, $\nabla_{ad} = (\partial \ln T / \partial \ln P)_s$, $\chi_T \equiv (\partial \ln P / \partial \ln T)_\rho$, and $\chi_\rho \equiv (\partial \ln P / \partial \ln T)_T$.

4.2.3 Relationship to the Riemann Solver-Based Hydrodynamics Implementation

When using the Riemann solver-based hydrodynamics capabilities described in the previous section, MESA does not cast the stellar structure equations in terms of local heating as in Equation 40. Instead, it combines Equation 40 with the constraint of fluid momentum conservation to form a local total energy equation.

We have the mass continuity equation

$$\frac{D\rho}{Dt} = -\frac{\rho}{r^2} \frac{\partial}{\partial r} (r^2 u) \quad (45)$$

and the momentum equation

$$\frac{Du}{Dt} = -\frac{1}{\rho} \frac{\partial P}{\partial r} - \frac{\partial \Phi}{\partial r} \quad (46)$$

written in Lagrangian form and assuming spherical symmetry. The variable u is the radial velocity and Φ is the gravitational potential. Thus, using these two equations along with equations 40 and 43, we get

$$\frac{D}{Dt}\left(e + \frac{1}{2}u^2 + \Phi\right) = \epsilon - \frac{\partial}{\partial m}(L + P\mathcal{A}u) \quad (47)$$

where $\mathcal{A} = 4\pi r^2$. This is the expression that MESA solves numerically.

5 MESA software

5.1 Installation procedure

- Download and install the right version of MESA SDK from [MESA SDK website](#).
- Download the latest MESA version from [here](#).
- Older MESA versions can be found [here](#).
- Setting up of environment variables:

```

1  # set MESA_DIR to be the directory to which you downloaded MESA
2  export MESA_DIR=/Users/user_name/Software/mesa-r15140
3
4  # set OMP_NUM_THREADS to be the number of cores on your machine
5  export OMP_NUM_THREADS=2
6
7  # you should have done this when you set up the MESA SDK
8  export MESASDK_ROOT=/Applications/mesasdk #basically path to the sdk folder
9  source $MESASDK_ROOT/bin/mesasdk_init.sh
10
```

These lines can be put in the `bashrc` or `bash_profile` which are during startup

- Compile MESA:

```

1  cd $MESA_DIR
2  ./install #./clean can be run before this if issues are faced
3
```

- We should perform and store our work somewhere other than the main MESA directory. To see if MESA is working, we can run a test. In a directory which will be used for working, make a copy of a pre-existing tutorial folder and run it through the following lines of code:

```

1  cp -r $MESA_DIR/star/work tutorial
2  cd tutorial
3  ./mk #compiles the work
4  ./rn #runs the code
5
```

- Further details can be found [here](#).

5.2 Importing and running the testsuite

The MESA testsuits is a handy source of examples, which provide the default inlists for a lot of different cases, albeit a simplistic model. You can find exhaustive details [here](#).

- The testsuites exist at -

```
1 $MESA_DIR/star/test_suite
2
```

Recall that MESA_DIR was where MESA lives on your desktop.

- From here, make a copy of any of these testsuites to your personal directory where you want to work with them, using the code-

```
1 cp -r $MESA_DIR/star/test_suite/name_of_test_suite your_personal_test_suite
2
```

- To use these outside the directory we need to change some things. First, we go into `make/makefile` and delete -

```
1 MESA_DIR = ../../../../
2
```

Then in the inlist file we delete the line

```
1 mesa_dir = ' ../../../../ '
2
```

- If any inlist calls any file with a relative path, we have to change it to make it an absolute path
- Finally, in your work directory, to compile and run MESA give the commands -

```
1 ./mk
2 ./rn
3
```

5.3 A small introduction to the different files

The most important module is “star”, which contains the module that knows how to put the capabilities of all the other modules together and advance the state of a stellar model by a single step and then suggest a new time increment for the next step.

The inlist is the master configuration file which is the file that MESA reads on starting up. In this file, there are 3 sections -

- `star_job` – options for the program that evolves the star
- `controls` – options for the MESA star module
- `pgstar` – options for on-screen plotting

There are of course a bunch of other inlist files, along with a useful file called `run_star_extras.f90` which contain very useful parameter, but are very testsuite dependent, and we shall see them later. The files that contain a description of all of the MESA options and their default values live in the directory

```
1 $MESA_DIR/star/defaults
```

5.4 Installing on cluster

- Go to the cluster scratch space
- Download MESA

```
1 svn co -r version_number http://mesa.svn.sourceforge.net/svnroot/mesa/trunk mesa
```

- Download the right version of MESA SDK and upload it to the cluster using cluster commands
- Edit the .bashrc:

```
1 export SCRATCH="/home/BHMG2/" #in our Noether cluster
2
3 # for MESA
4 export MESA_DIR=$SCRATCH/mesa
5 export MESASDK_ROOT=$SCRATCH/mesasdk
6 source $MESASDK_ROOT/bin/mesasdk_init.sh
7
```

- As before cd into MESA_DIR and run ./install

5.5 Running MESA jobs on cluster

For this, the following two links are quite helpful: [single jobs](#) and [many jobs](#)

5.5.1 Single Jobs

- Copy the correct test-suite from the main MESA directory and make the relevant changes to run it outside the MESA directory. Call this your work directory
- cd into it and run ./mk to compile.
- In the work directory, make a batchfile and call it runmesa.sh:

```
1 #!/bin/bash
2 #PBS -N mesa_PPISN
3 #PBS -q longq/default
4 #PBS -l nodes=1:ppn=8
5 #PBS -o out.log
6 #PBH -e err.log
7 #PBS -S /bin/bash
8 #
9 cd $PBS_O_WORKDIR
10
11 #
12 # this should be equal to the value of ppn
13 # here we have assigned 8 cores
14 #
15
16 export OMP_NUM_THREADS=8
17
18 ./rn
```

- Submit the batchfile using qsub runmesa.sh

5.5.2 Many Jobs

This is a guide to setting up MESA inlists when many jobs need to be run for different parameter stars

- Create a work directory called **base** and copy the required inlist files that do not change between the models
- Alter the main inlist file in the base directory and set absolute paths in the function calls to the different files

```
1 &star_job
2
3     history_columns_file = '/home/BHMG2/ppisn_sim/many_jobs_old/base/
4     history_columns.list'
5     profile_columns_file = '/home/BHMG2/ppisn_sim/many_jobs_old/base/
6     profile_columns.list'
7     read_extra_star_job_inlist1 = .true.
8     extra_star_job_inlist1_name = '/home/BHMG2/ppisn_sim/many_jobs_old/base/
9     inlist_ppisn'
10
11 / ! end of star_job namelist
12
13 &controls
14
15     read_extra_controls_inlist1 = .true.
16     extra_controls_inlist1_name = '/home/BHMG2/ppisn_sim/many_jobs_old/base/
17     inlist_ppisn'
18
19 / ! end of controls namelist
20
21 &pgstar
22
23     read_extra_pgstar_inlist2 = .true.
24     extra_pgstar_inlist2_name = '/home/BHMG2/ppisn_sim/many_jobs_old/base/
25     inlist_ppisn'
26
27 / ! end of pgstar namelist
```

- Now create cluster inlists that vary between the runs. Here make another directory called **runs**. This directory contains folders that have been named with different masses. These contain the inlist files that vary between the runs. For example, in our case **runs/42** contains the **inlist_extra** file that specifies the star mass to be $42M_{\odot}$. Other files that haven't been given absolute path can also be added here.

```
1 &controls
2     initial_mass = 42.00d0
3 / ! end of controls namelist
4
```

- Submission script (**cluster.sh**):

```
1 #!/bin/bash
2 #PBS -N mesa_PPISN
3 #PBS -q longq/default
```

```

4  #PBS -l nodes=1:ppn=8
5  #PBS -o out.log
6  #PBH -e err.log
7  #PBS -S /bin/bash
8  #PBS -t 40 42 44 46 48 50 52 54 56 58 60 62 64 66 68 70 72 74 76 78 80 82 84
   86 88 90
9
10 #Set variables
11 export MESA_DIR="/home/BHMG2/mesa-r12778"
12 export OMP_NUM_THREADS=8
13 export MESA_BASE="/home/BHMG2/ppisn_sim/base" #absolute path to base folder
14 export MESA_INLIST="$MESA_BASE/inlist" #path of main common inlist to be
   read
15 export MESA_RUN="/home/BHMG2/ppisn_sim/runs" #absolute path of the runs
   folder
16
17 #CD to folder
18 cd $MESA_RUN/$PBS_ARRAYID "
19
20 #Run MESA
21 $MESA_BASE/star
22

```

- Submit the jobs by executing `qsub cluster.sh`

5.6 Storage of MESA data

By default, MESA stores its data in the `./LOGS` directory. The data files are text-based and can be fed into any plotting program. In the LOGS directory, the main files are -

- **history.data**: The history for the run is saved, one line per logged model, in the file “history.data”. The first line of history.data has column numbers, the second line has column names, and the following lines have the corresponding values. The model numbers will not monotonically increase, since after a backup or a restart the new model numbers and lines are appended.
- **profile.index**: MESA doesn’t store profiles for every step. This list tells us how to translate between the numbers in the profile filenames and the MESA model numbers. By default, MESA will store a profile at the end of the run. For each profile, there is a line in profiles.index giving the model number, its priority, and its profile number. Priority 1 is controlled using the `profile_interval` parameter, and Priority 2 is for special events in evolution.
- **profile.data**: The profiles contain detailed information about a selected set of models, one model per file. Each profile includes both a set of global properties of the star, such as its age, and a large set of properties for each point in the model of the star given one line per point. In each case, the lines of data are preceded by a line with column numbers and a line with column names.

We can use the `history_columns.list` and `profile_columns.list` in `$MESA_DIR/star/defaults/` to add/remove the columns of interest, but if we want something which is not in the list, we will have to use `run_star_extras.f`.

5.7 Extracting data using PyMESARReader

`mesa_reader` is a module consisting of three classes that we use to read in the contents of a LOGS directory. There are three classes are called `MesaData` : corresponds to data in profiles or history files, `MesaProfileIndex` : corresponds to data found in profiles.index, and `MesaLogDir` : which ties together data in profiles, the profile index, and the history file.

For example, sample code to load in a specific column/star variable of interest is -

```
1 # import mesa_reader to make its classes accessible
2 import mesa_reader as mr
3
4 # make a MesaData object from a history file
5 h = mr.MesaData('LOGS/history.data')
6
7 # extract the star_age column of data
8 name_of_array = h.name_of_variable_asin_history.data
```

Similarly, to load profiles by their associated model number and also to load the last saved profile -

```
1 import mesa_reader as mr
2 l = mr.MesaLogDir('./LOGS')
3
4 # load the profile associated with model number 100
5 p_100 = l.profile_data(model_number=100)
6
7 # load the profile with PROFILE number 12
8 p_12 = l.profile_data(profile_number=12)
9
10 # load the last profile saved (largest model number)
11 p_last = l.profile_data()
```

6 Different stages in MESA important for PPISN

6.1 Introduction to the PPISN testsuite

As usual, we have the general inlist files, which has the `star_job`, controls and `pgstar` details of the files to load in it. The main inlist here is of the `inlist_ppisn`, which has the most important controls need to vary the runs, ranging from the maximum number of model numbers, retries, mass of star, adjustments to the newton solver, convection and overshoot controls, termination conditions, timestep options, central abundances, mesh controls, EOS controls and finally the additional parameters used to turn hydro on and off which is explained in greater detail below.

The `inlist_extra` is used to describe the ZAHB mass of the bare helium core we wish to evolve. The `inlist_hydro_on` simply turns off the wind, and uses the hydrodynamic of the T gradient and momentum equations as described earlier in detail. The `inlist_hydro_off` turns on the wind back, and stops using the momentum equations. As usual, the `star` (executabe file), the `mk` (compilation of inlists), `rn` (running of the actual model), and `re` (to load a previous model and then run) are in this testsuite too, same as others.

The LOGS usually contain the `history.data`, the `profiles.index`, and the profile models. It also stores model as a `.mod` extension, usually during `prehydro`, or `PISN`.

6.2 Pulsation evolution using HLLC

Shocks are modelled using MESA’s HLLC contact solver. This is only used when star evolves away from hydrostatic equilibrium (recall 4). Time just before a pulse (when MESA decides to switch to HLLC) is defined to be when the pressure weighted integral $\langle \Gamma \rangle < 4/3$. Hydrodynamic equations are non linear, and the initial conditions for the generation of a shock are energy injections into specific cells which physically correspond to explosive oxygen burning in the case of PPISN.

For the Riemann hydro solver to be turned on in the PPISN module (version r12778), the following conditions are met:

- The temperature of the core is greater than 10^9 K (`x_cntrl(1)`)
- $\langle \Gamma \rangle < 4/3$ (`x_cntrl(2)` < 0.01)
- If the neutrino luminosity is above 10^{10} (`x_cntrl(3)` > 10). This condition is independent of the first two conditions

Other parameter controls important to the physics of the problem:

- `x_cntrl(4)`: velocity in km/s at any zone for which we consider the system to be undergoing a pulse
- `x_cntrl(8)` is the control parameter which sets the mass fraction within which additional conditions must be met. This increases the time after a set timescale parameter so that additional shocks (which are mostly reflections of the inward propagating shocks at the base of the model) reach the surface.
- `x_cntrl(7)` When its time to remove the outer layers, all mass above any layer that reaches the escape velocity times this factor will be removed. This is of course after secondary shocks have reached the surface

(Side note : The condition for angular frequency going imaginary in the asteroseismology g-mode frequency (buoyancy frequency) does not imply overall dynamical instability. It is just a local condition that indicates the onset of convection (no oscillation)). After the material is excised, a new stellar model with same mass, chemical composition, and entropy as the previous model (minus the excised material) is created. It is imperative to know that mass loss due to winds are ignored during the hydrodynamics phase. After the new model is created, MESA goes back to the hydrostatic solver, since it is now in hydrostatic equilibrium, unless another pulse occurs, or core collapse occurs.

7 Reproduced figures

7.1 Lower edge of the mass gap

The conditions used to determine the various masses are as follows:

- Star mass at He depletion is found when `center_he4` ($X(\text{He})$) a parameter present in `history.data` goes below 10^{-3} (This is as defined in MESA, unlike [7] who use 10^{-2}).
- CO core mass is defined as the region in the core of the star where $X(^4\text{He}) < 0.01$ and $X(^{12}\text{C}) + X(^{16}\text{O}) > 0.01$. This is captured by `co_mass`, a parameter present in `history.data`. (Again, [7] just use the first condition, whereas [10] use both the conditions).

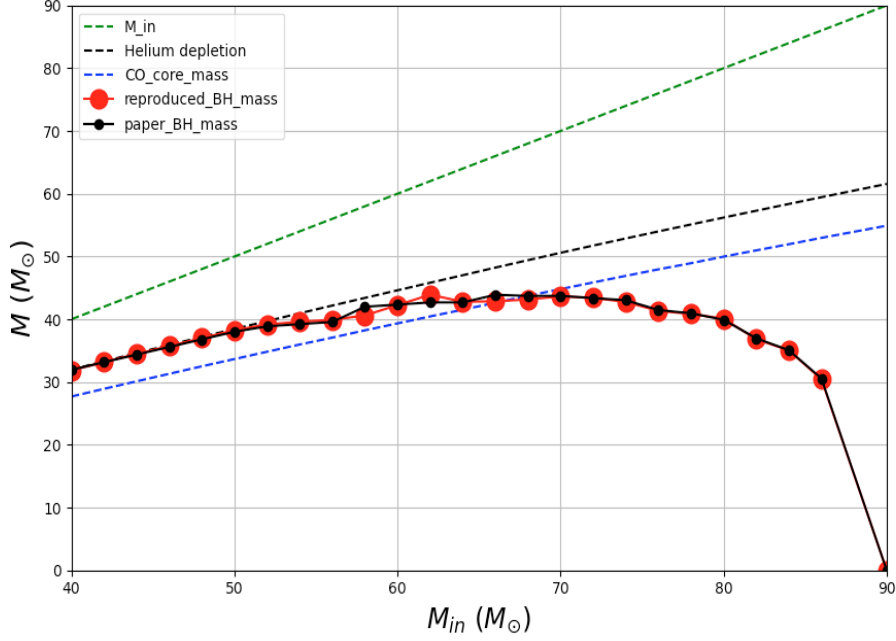


Figure 19: Final BH mass (M_{BH}), star mass at He depletion (M_{He}), CO core mass at He depletion (M_{CO}) plotted as a function of initial mass (M_{in}) for stars of metallicity $Z_{\odot}/10 = 0.00142$. The compared BH masses are from [33]

- The PPISN module, terminates evolution at iron core collapse. This is decided through the parameter `fe_core_infall_limit` which specifies the max speed of infall of any layer interior to the `fe_core_mass`, which we set to be $8d8$ cm/s (as given default).
- The final black hole mass at this stage is decided through 2 conditions: all layers that have velocities less than escape velocity and the mass that has a gravitational binding energy of $> 10^{48}$ ergs. Authors of [10] consider both the conditions whereas the authors of [33] consider only the escape velocity condition.

An extra point on the final assumption of binding energy of $> 10^{48}$ ergs. We follow authors in [11]. They define 2 time scales, the free fall timescale as $t_{ff} = (r^3/GM(r))^{1/2}$ and the timescale t_{ν} of change in gravitational mass δMG due to neutrino emission. Regions in the collapsing star for which $t_{ff} < t_{\nu}$ fall on to the black hole without experiencing any significant change in their gravitational acceleration and regions that satisfy $t_{ff} > t_{\nu}$ respond instantaneously to the change in gravity.

Once neutrinos change the gravitational mass, the inward gravitational force on each mass shell has decreased and thus there is a net outward acceleration due to the excess pressure gradient. The characteristic radius for where this shock pulse thus forms is r_c where $t_{ff} = t_{\nu}$. This is around 10^9 cm. This outward acceleration produces a velocity and the KE of the shock is what is imparted to the next mass shell. At r_c this comes out 10^{48} ergs conservatively, and this KE decreases as the

shock is propagated, thus a more correct version is the analytic one as derived in the paper as -

$$\text{KE} = 10^{48} \frac{\alpha H (\delta M G)^2 2 * 10^9}{0.16 (0.3 M_{\odot})^2 r^2} \text{erg}$$

where $\alpha = d \ln M / d \ln r$ and H is the pressure scale height.

Results from MESA runs:

For normal stars with metallicity $Z = Z_{\odot}/10 = 0.00142$

- The lower edge of the mass gap lies at $43.9 M_{\odot}$ for ZAHB mass $62 M_{\odot}$
- The upper edge of the mass gap lies at $123.96 M_{\odot}$ for ZAHB mass $242 M_{\odot}$

7.2 Miscellaneous plots

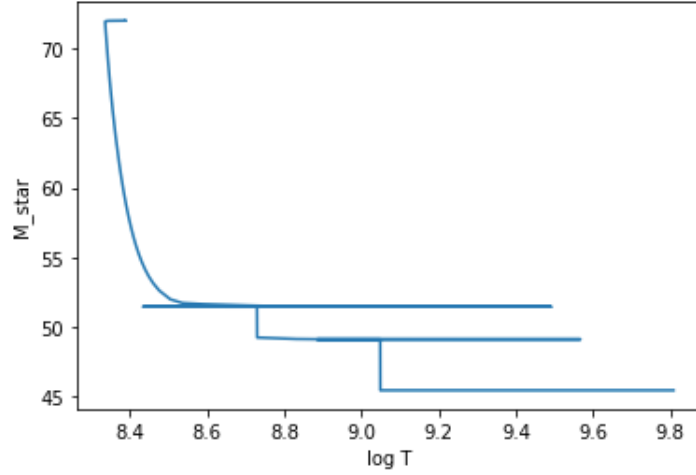


Figure 20: Star mass as a function of central temperature for a star of initial mass $72 M_{\odot}$ (central temperature is used as an indicator of age). The gradual decline in mass indicates mass loss due to winds whereas the sudden drops in mass indicate mass loss due to pulsations.

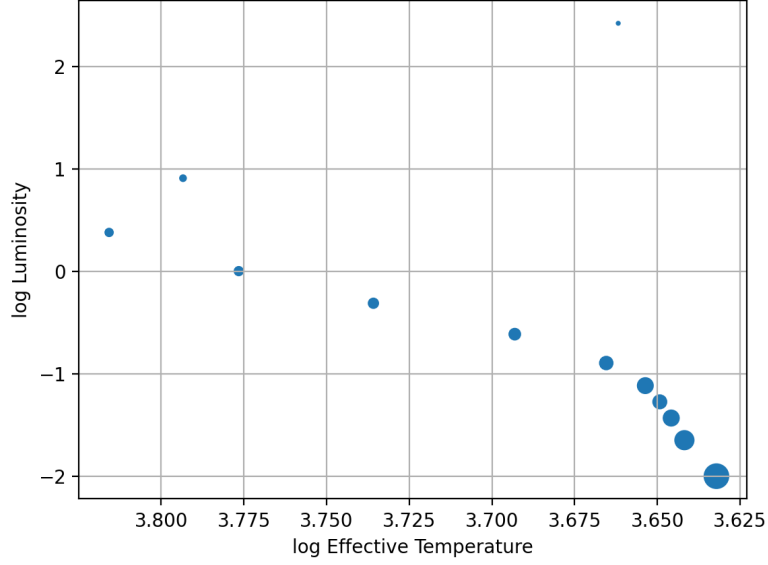


Figure 21: An observational HR diagram obtained using MESA for $0.2 - 1.1M_{\odot}$ in steps of $0.1M_{\odot}$, $1.17M_{\odot}$, and $1.19M_{\odot}$. The size of the circles correspond to Kroupa IMF.

7.3 Attempt at the instability region

Recall the main derivations of the instability region -

7.3.1 Thermodynamics

Here, we look for regions in the $T_c - \rho_c$ (central temperature and density) plane where the adiabatic index $\Gamma_1 < 4/3$

$$\Gamma_1 = \frac{\rho}{P} \left(\frac{\partial P}{\partial \rho} \right)_s = \frac{\rho}{P} \left[\left(\frac{\partial P}{\partial \rho} \right)_T + \left(\frac{\partial P}{\partial T} \right)_\rho \left(\frac{\partial T}{\partial \rho} \right)_s \right] \quad (48)$$

with

$$\left(\frac{\partial T}{\partial \rho} \right)_s = - \frac{(\partial s / \partial \rho)_T}{(\partial s / \partial T)_\rho} \quad (49)$$

where s is the entropy per unit mass throughout. We now look at contributions to the pressure and entropy due to individual species

7.3.2 Ions

The relevant thermodynamic relations for these objects are the ideal gas law and the Sackur-Tetrode equation:

$$P_{ions} = \left\langle \frac{1}{A} \right\rangle \frac{\rho k_B T}{m_H} \quad (50)$$

$$\text{and } s = \left\langle \frac{1}{A} \right\rangle \frac{k_B}{m_H} \left[\frac{5}{2} + \ln \left(\frac{T^{\frac{3}{2}}}{\rho} \right) \right] \quad (51)$$

where $\langle 1/A \rangle$ is the average reciprocal atomic unit.

7.3.3 Radiation

In this case, the relevant quantities are the radiation pressure and the radiation entropy:

$$P_{rad} = \frac{a}{3} T^4, \quad \text{and} \quad s = \frac{4}{3} a \frac{T^3}{\rho} \quad (52)$$

7.3.4 Electrons and Positrons

Define

$$C_e = \frac{1}{\pi^2} \left(\frac{m_e c}{h} \right)^3, \quad \beta_e = \frac{m_e c^2}{k_B T}, \quad \text{and} \quad \phi = \frac{\mu}{k_B T} \quad (53)$$

with μ as the chemical potential, determined by the condition of charge neutrality. It is imposed by demanding that the excess is due to ionization, that is $n_{e^-} - n_{e^+} = \langle Z/A \rangle \rho$, and using this to find μ by equating to n_e as below - The pressure, density, charge density, and entropy as follows:

$$P_e = m_e c^2 C_e F_1 \quad (54)$$

$$\rho_e = m_e C_e F_2^+ \quad (55)$$

$$n_e = C_e F_2^- \quad (56)$$

$$s_e = \frac{k_B C_e}{\rho} (F_1 + F_3 - \frac{\phi}{\beta_e} F_2^-) \quad (57)$$

$$u_e = m_e c^2 C_e F_3 \quad (58)$$

Where the integrals are defined as -

$$F_1 = \int_{\epsilon=\beta_e}^{\infty} \Gamma\left(\frac{\epsilon}{\beta_e}\right) D^+ \frac{d\epsilon}{\beta_e} \quad (59)$$

$$F_2 = \beta \frac{dF_1}{d\phi} \quad (60)$$

$$F_2^+ = \int_{\epsilon=\beta_e}^{\infty} \Gamma'\left(\frac{\epsilon}{\beta_e}\right) D^+ \frac{d\epsilon}{\beta_e} \quad (61)$$

$$F_2^- = \int_{\epsilon=\beta_e}^{\infty} \Gamma'\left(\frac{\epsilon}{\beta_e}\right) D^- \frac{d\epsilon}{\beta_e} \quad (62)$$

$$F_3 = \int_{\epsilon=\beta_e}^{\infty} \epsilon \Gamma'\left(\frac{\epsilon}{\beta_e}\right) D^+ \frac{d\epsilon}{\beta_e} \quad (63)$$

$$(64)$$

with $\epsilon = \frac{E}{k_B T}$,

$$\Gamma = \frac{(x^2 - 1)^{3/2}}{3}, \quad \text{and} \quad D^\pm = \frac{1}{e^{\epsilon - \phi} + 1} \pm \frac{1}{e^{\epsilon + \phi} + 1} \quad (65)$$

We can also determine the ratio between the total number of leptons (electrons and positrons) to the electric charge of the leptons (measured in units of the electron charge) written as ν as -

$$\nu = \frac{F_2^+}{F_2^-} \quad (66)$$

Finally, as we now know the partial pressures, densities and entropy of all the ions, electron positron pairs and radiation, we can plug it into eq (1) to find the Γ and decide if there is an instability or not.

7.3.5 Attempt on Mathematica

The main unknown which we have yet to determine is μ , the chemical potential. For this, we need to solve $\rho_c/2 = C_e * F_2^-$. Our initial attempt was to simply do this using the Solve Function, and then compute Γ_1 , but it was too computationally heavy for Mathematica to do.

```
1 Solve[F2minus == rhoc/(2*Ce), mu]
2 Gamma1 = (rhoc/P) * (D[P, rhoc] - D[P, Tc]*D[S, rhoc]/D[S, Tc])
```

The next (and current) attempt is to first NIntegrate F_2^- , and form a table to invert it so as to solve for μ , by expanding it around 0. We are currently still looking into this aspect.

8 Literature survey

8.1 Astrophysics papers

8.1.1 Accretion in Binaries [37]

The paper examines whether BHs can pollute the gap after accreting from a stellar companion. It considers the possibility of forming BBH mergers in isolated binaries where at least one of the components has a mass within the PISN mass gap ($M_{BH} > 45M_\odot$; PISN mass gap events). Apart from discussing the super-Eddington accretion rate, which forms the basis for simulations, the paper also discusses other pathways to PISN mass gap events such as: consecutive mergers of BHs, fallback of a H-rich envelope (as opposed to ejection), accretion from the interstellar medium, and primordial BHs.

The paper provides a detailed description of the model used for simulation (using a population synthesis code called COMPAS) and compares/distinguishes the results of simulations with the predictions from the other pathways. Under their most extreme assumptions, the authors find that about 2% of BBH mergers are PISN mass gap events and the maximum mass for a BH involved in a PISN mass gap event is $M_{BH,max} = 90M_\odot$.

8.1.2 Astrophysical Implications of GW190521 [1]

GW190521 with its unusually high component masses, had a 99% probability that atleast one of the BHs falls in the mass gap predicted by pair-instability supernova theory. In this paper, the authors assume the source to be the coalescence of a quasi-circular compact binary system. The paper provides details about the Bayesian parameter estimation procedure and the posterior probability

distributions that provide estimates of the source’s intrinsic and extrinsic parameters. It further quantifies the evidence for orbital precession.

The authors discuss the consistency of the residual data from the observed signal in different regions such as merger and ringdown with expectations from waveform models derived from GR. The paper also estimates a merger rate similar to GW190521, and discusses the implications for stellar collapse by examining the uncertainties in PI and stellar evolution theory, the heirarchical merger scenario (mergers involving 1 or 2 second generational BHs), the stellar merger scenario, and the AGN disk scenario. It also discusses some alternate scenarios such as strong gravitational lensing and eccentricity of mergers that may have been responsible for such a GW wave signal.

8.1.3 Formation of Binary Black Holes Similar to GW190521 [17]

In the case of zero-metal (Pop III) stars, the authors show that the total mass of binary black holes from binary Pop III star evolution can be $150M_{\odot}$, which agrees with the mass of the binary black hole GW190521. The paper includes a detailed analysis of the effect of rotational velocity of Pop III stars at ZAMS. It also discusses the evolution of Pop III binaries (which tend to retain envelopes due to lack of metals) using population synthesis simulations for various models with different initial conditions: initial mass function, initial mass ratio, separation and eccentricity distributions of binaries, binary evolution parameters such as mass transfer rate of the donor, fraction of transferred stellar mass in the accretion process, common envelope parameters, and tidal coefficient factor.

The authors plot remnant mass with and without PPISN as a function of M_{ZAMS} , and primary and secondary BH mass distributions for binary BHs with and without PPISN, comparing it with the GW190521 predictions of both, demonstrating consistency. The various population parameters/uncertainties involved in these computations are also outlined. The paper concludes with a review of what other papers in the field have studied/considered, shortcomings, and its implications in the context of GW190521.

8.1.4 BH population analysis [2]

The authors introduce a novel, 3-parameter, black hole mass function which realistically models the physics of pair instability supernovae. The function has a single dimensionful parameter, $M_{BHM\bar{G}}$, which reveals the location of the lower edge of the BHM \bar{G} . This is obtained by applying the mass function to all events in the LIGO-Virgo GWTC-2 catalog, wherein a distinctive peak ($M_{BHM\bar{G}}$) is observed for the lower edge of the mass gap. The mass gap manifests itself as a discontinuity in the mass function and is populated by a distinct, less abundant population of higher-mass black holes.

The authors use the BBH (binary black hole) events detected by LVC (LIGO-Virgo) to constrain the parameters of their population model (through Bayesian statistics) and establish that the mass function fits a new catalog of black hole masses approximately as well as pre-existing phenomenological mass functions. They also remark on the implications of their results for constraining or discovering new phenomena in nuclear and particle physics.

8.1.5 Collisions & BHM \bar{G} [19]

The paper explores in detail the formation of BHs with masses within or above the pair-instability gap through collisions of young massive stars in dense star clusters. The computational methods exploring a variety of physical assumptions pertaining to growth through stellar collisions, including

primordial cluster mass segregation (increased concentration of massive stars near the center) and the efficiency of envelope stripping during collisions, are discussed (computations using **Cluster Monte Carlo**). The various evolutionary outcomes (which uniquely depend upon stellar collisions and will never occur through single star evolution for the assumed IMF) such as PI gap BH, IMBH, and PISN for massive stars undergoing collisions in star clusters are also discussed.

It is found that as many as 20% of all BH progenitors undergo one or more collisions prior to stellar collapse and up to 1% of all BHs reside within or above the pair-instability gap through the effects of these collisions. The authors analyse the implications of this in GW astronomy in the context of GW190521. The cosmological rates of PISNe and other electromagnetic transients are also studied.

8.1.6 Convection dependence of BHMg [30]

The most massive BH progenitors experience episodic mass ejections on time-scales shorter than the convective turnover time-scale, invalidating the steady state assumption required for the classical mixing length theory. The aim of the paper is to stimulate improvements in stellar evolution models that also account for the time-dependent behaviour of convective motion. The paper compares the final BH masses computed with two different versions of the stellar evolutionary code MESA: (i) using the default implementation of Paxton et al. (2018) and (ii) solving an additional equation accounting for the time-scale for convective deceleration.

In the second version, it is found that stronger convection develops during the pulses and carries part of the energy, leading to weaker pulses. This leads to lower amounts of mass being ejected and thus higher final BH masses of up to $5M_{\odot}$. However, the differences were much smaller for the progenitors that determine the maximum mass of BHs below the gap (leaving the mass gap virtually unchanged). This is an encouraging indication that current models are robust enough for comparison with the present-day gravitational-wave detections. The paper also looks at some alternate treatments of time-dependent convection.

8.1.7 Core collapse after PPISN [29]

The paper presents 3D core-collapse supernova simulations of massive Pop-III progenitor stars at the transition to the pulsational pair instability regime. Simulations involve two progenitor models with initial masses of $85M_{\odot}$ and $100M_{\odot}$ with the LS220, SFHo, and SFHx equations of state. The authors describe the numerical methods and setup for simulating the two progenitor models in detail. The 3D explosion dynamics are modelled using spherical harmonics to trace the angle-dependent shock positions.

It is found that the $85M_{\odot}$ progenitor experiences a pair instability pulse coincident with core collapse, whereas the $100M_{\odot}$ progenitor has already gone through a sequence of four pulses 1,500 years before collapse in which it ejected its H and He envelope. The paper also analyses the strong gravitational waves produced by these two events both in the high-frequency g-mode emission band and at low frequencies, and looks at the detection prospects of these waves.

8.1.8 Effect of Overshoot on BHMg [35][36]

In these papers, the authors study the sensitive effect of the convective overshoot parameter on the BHMg and calculate the mass ejection of Population III stars by the pulsational pair-instability

(PPI) process using a stellar evolution and hydrodynamical code (BSE and HOSHI code). It was found that the lower bound of the gap can be much larger than previously thought if a relatively small, but reasonable, overshooting parameter was adopted.

The general findings of the two papers are that due to the low overshoot parameter, the stars do not become red super giants during the PPI phase, and in this case most of the hydrogen envelope remains after mass ejection by PPI, leading to heavier BHs. The paper also conducts population studies of Pop-III BH-BH merger rate densities. Furthermore, this paper also studies the effect of the overshoot parameter specifically in the context of GW190521 and discusses its implications.

8.1.9 Effect of Reaction Rates on BHMg [6]

This paper investigates the main uncertainties on the PI mass gap: the CO reaction rate and the H-rich envelope collapse (Here we assume that the massive star retains its H rich envelope and if it collapses to the final BH, this can radically alter the BHMg). Pure He stars with masses between $20 - 100M_0$ with $Z = 0.001$ were evolved, and then with H envelopes with masses $40 - 160M_0$ and $Z = 0.0003$.

The main aim of the paper is to offer an explanation for the $85M_\odot$ primary component of GW190521. The parameters explored are uncertainties in the $^{12}\text{C}(\alpha, \gamma)^{16}\text{O}$ reaction rates, consideration of H-rich envelope at low metallicities, and convection/mixing to describe a dredge-up episode. The authors give a detailed description of their model implementation through the PARSEC code, wherein they vary the $^{12}\text{C}(\alpha, \gamma)^{16}\text{O}$ within 1σ uncertainties for pure Helium cores (mass gap $\sim 80M_\odot - \sim 150M_\odot$).

In the next section, the authors give their description of the H-envelope and consider a dredge up episode in massive stars during core He-burning that extracts matter from the core, enriching the envelope. Incorporating this and a 2σ uncertainty in $^{12}\text{C}(\alpha, \gamma)^{16}\text{O}$, they obtain the mass gap to be $92M_\odot$ to $110M_\odot$. Strikingly, in models computed with 3σ uncertainties, the mass gap is found to be completely removed by the dredge up effect. The onset of the dredge-up is found to be particularly sensitive to the assumed model for convection and mixing.

For pure He stars, within the range of $CO - 3\sigma$ to $CO + 3\sigma$ the lower edge varies from $20 - 68M_0$. With the normal CO rate, assuming H collapse the gap can go from $60 - 70M_0$. For $CO - 1\sigma$ rate, PISN gap ranges from $80M_0 - 150M_0$. For $CO - 2\sigma$ rate PISN gap ranges from $90 - 110M_0$. With the rate of $CO - 3\sigma$ the mass gap is completely removed.

8.1.10 Effect of Rotation on BHMg [24]

In this paper they study the effect of rotation on the hydrodynamics of PISN and PPISN. They perform simulations of nonrotating and rapidly rotating stripped helium stars in a metal-poor environment ($Z_0/50$) in order to resolve the lower edge of the upper mass-gap.

The effect of rotation on the hydrodynamics of PPISNe and PISNe can be understood in terms of two different effects that are produced by centrifugal support: a modification of the stability criterion ($\Gamma_1 < \frac{4}{3} - \frac{2\omega^2}{9} + O(\omega^4)$, where $\omega = \Omega/\sqrt{GM/r_e^2}$, where Ω is the rotational frequency and r_e is the equatorial radius), and that rotating stars follow an evolution that resembles that of lower mass stars (it lowers the value of T_c at a fixed ρ_c).

The inclusion of the ST dynamo in stripped stars leads to nearly solid-body rotation and efficient loss of angular momentum from winds. Without rotation, we find that PPISNe occur for masses

between $36 - 62M_0$. With ST dynamo it shifts to $37 - 64M_0$ and without to $43 - 76M_0$. Meanwhile for PISN, the lower edge for non rotating is $45M_0$ and for rotating with ST is $47M_0$ and without is $52M_0$.

8.1.11 Helium Burning and CO reaction rates [9]

A brief summary of stellar evolution - On the main sequence, hydrogen burning fuses four hydrogen nuclei into helium releasing about 25 MeV of energy. In massive stars $M > 1.5M$, the importance of the pp-chains is diminished and the fusion process is dominated by the CNO cycles. This results in the conversion of hydrogen to 4He and enrichment of ^{14}N based on the depletion of the initial ^{12}C and ^{16}O nuclei.

Hydrogen burning continues only in a shell surrounding the inert core. The hydrogen depleted core contracts gravitationally, increasing the density and temperature of the core matter. Helium burning is triggered by the 3α process producing ^{12}C . This is followed by the subsequent α capture reaction converting ^{12}C to ^{16}O . The ratio of $^{12}\text{C}/^{16}\text{O}$ is determined by the competition between the 3α and ^{12}C ^{16}O reaction rates at a given temperature.

In massive stars, as the convective helium core evolves the temperature and density rise significantly, and thus so does the energy generation due to the 3α process and ^{12}C - ^{16}O reactions. Carbon production is favored by larger densities and smaller CO reaction rate, while oxygen production is favored for smaller densities and larger CO reaction rate.

8.1.12 Likelihood of GW190521 under mass and spin priors [27]

They consider the 8-dimensional intrinsic parameter space spanned by the constituent BH masses and dimensionless spins and the extrinsic parameters constitute the 7-dimensional space of sky location (right ascension and declination, luminosity distance, orbital orientation with respect to the line of sight (LOS) at some reference epoch (polar and azimuthal angles of the LOS in the source frame), the angular degree of freedom about the LOS and the time of merger.

Monte Carlo (MC) integration of the Bayesian evidence is used to sample the posterior distribution over the full 15-dimensional space of parameters. A natural choice would be to draw spins from independent isotropic distributions and masses from distributions that are uniform over large ranges to be as nonrestrictive as possible. For the extrinsic parameters they use geometric priors, being isotropic in all the BBH and detector orientation angles.

LVC parameter estimation found that the most likely scenario for GW190521 was an equal-mass ($q \lesssim 0.3$) BBH with both constituents falling inside the (pulsational) pair instability mass gap, and that the binary's effective spin was consistent with zero. GW190521 source parameters are extremely sensitive to the uninformative priors taken. Parameters that fit the data well either place at least one BH inside the mass gap or avoid the gap with a mass ratio far from unity and a precessing primary spinning opposite the direction of the orbit (the latter which requires extremity special circumstances to make). One might consider the Bayesian evidence of GW190521 under mass and spin priors describing the BBH merger population in AGN disks.

8.1.13 Max BH mass across cosmic time [38]

Using MESA, the paper shows that for stellar models with non-extreme assumptions, $90..100 M_\odot$ stars at reduced metallicity ($Z/Z_\odot < 0.1$) can produce blue supergiant progenitors with core masses

sufficiently small to remain below the fundamental pair-instability limit, yet at the same time lose an amount of mass via stellar winds that is small enough to end up in the range of an "impossible" $85 M_{\odot}$ black hole. The key points are the proper consideration of core overshooting and stellar wind physics with an improved scaling of mass loss with iron (Fe) contents characteristic for the host galaxy metallicity.

The prime reason this solution was not considered until the discovery of GW 190521 was that previous authors generally assumed the H-envelope to be lost, either due to binary Roche-Lobe overflow or strong mass loss in an individual star, e.g. as a Luminous Blue Variable (LBV). The authors argue that there is no a priori reason to assume that very massive stars (VMS) lose their H-envelopes. The paper contains a detailed description of MESA modelling including an improved treatment of wind mass loss. It also discusses potential extra mass loss near the Eddington Limit. The authors look at the role of metallicity and discuss "silent collapse of a star" i.e. core-collapse without supernova explosion (avoiding considerable mass loss!), before ending the paper with a summary and outlook.

The key conclusion of the paper is that for low- Z host galaxies it is possible to create first generation BHs up to values as large as $90 M_{\odot}$, without the need to invoke second generation BH formation, extreme assumptions, or exotic physics.

8.1.14 Modified Gravity and BHMg [33]

They postulate that independent of the specific mechanism, in an unscreened environment the effective value of the gravitational constant would be changed to $G = (1 + \frac{\Delta G}{G_N})G_N$, with G_N being Newtons Constant. They numerically simulate the evolution of population-III stars from (ZAHB) to either core collapse or PISN, finding that increasing G results in a stronger instability, increasing the mass loss during pulsations, forming lighter BH's.

These different G affect the structure and evolution of the star, which is altered because the pressure support required to maintain hydrostatic equilibrium is increased, since $d\frac{dP}{dr} = -\frac{GM\rho}{r^2}$. From dimensional analysis, we find $\log(T_c) \propto \log(G)$. The effect of increasing G at fixed mass is then to raise the central temperature at fixed central density, implying that tracks in the $\log(T_c)$ - $\log(\rho_c)$ plane pass closer to the instability region. The ultimate result of the altered stellar evolution is then to lower the edges (both upper and lower) of the BHMg.

The escape velocity also increases, retaining more mass and hence raising the gap. Increasing G reduces the helium burning lifetime, which results in less wind mass loss, and increasing the ratio of C/O, quenching pulsations and resulting in heavier BH.

Running for $-0.35 < \frac{\Delta G}{G_n} < 0.5$, they find that the most important effect of changing G is the first one, resulting in less mass BH. They use the specific values motivated by obtaining a bound on the ratio of the gravitational constant experienced by blackholes and baryonic matter. They then test the LIGO/VIRGO obtained data with this, and find that this can explain the GW190521 discovery too.

8.1.15 PBH and BHMg [8]

To check primordial origin of GW190521, we need to check if the merger rate is in agreement with observations and with the primordial BH mass function according to current constraints. We consider 2 scenarios - first assumes that this event is the only one of primordial origin among the LIGO/Virgo catalogues; the second supposes that all GW events observed so far are primordial.

GW190521 as a single PBH event without accretion

There is a tension in the f_{PBH} as found from those by CMB distortions, and it would be an outlier of the population with a corresponding merger rate orders of magnitude below the observed one.

GW190521 as a single PBH event with accretion

Here, the value of f_{PBH} agrees with those allowed by experiments. Further, if we assume that all events by LIGO/VIRGO are primordial, then the results are compatible as predicted by the population. Even the inferred values of the binary components' spins are consistent with the accreting PBH scenario.

8.1.16 Pulsational Pair-instability Supernovae, Pre-collapse Evolution and Pulsational Mass Ejection [23]

They study PPI which occur in the He-core of M_{He} from 40-64 M, which are the cores of 80 – 140 Main-sequence stars. With metallicities 0.01-1Z, stars with a higher metallicity have a stronger stellar wind mass loss, thus forming a smaller mass He-core. In order for the star to form a He-core of more massive than 40 M and thus to undergo PPI, $Z < 0.5$ is required.

They probe $Z=0$, undergoing PPI, with total ejected mass almost a monotonically increasing function of M_{He} except for some fluctuations in the lower mass end. The number of pulses ranges from 6 weak pulses for $M_{He} = 40$ M to no weak pulse but 2 strong pulses for $M_{He} = 62M$. The ejecta mass is lower than 1 M in the low mass end and increases to as large as 10M near the PISN regime. The ejecta form circumstellar matter (CSM). The lower mass He-cores with $M_{He} = 55M$ eject only the He-envelope. More massive cores eject a part of the CO layer. The most massive core studied of $M_{He} = 62M$ ejects even the Si-layer. Such heavy elements may largely alter the opacity of the CSM.

They also show that PPISN model produces a massive enough CSM which can explain superluminous supernovae.

They find the lower edge to be $52M$.

8.1.17 PPISN-Astrophysics [39]

The paper starts off with a discussion on the physics of pulsational pair instability (PPI). This includes the physics used in the KEPLER code which is used to model all stars and explosions. As the outcome of the PPI depends critically upon the helium core mass, some time is spent reviewing the outcome of instability and explosion in bare helium cores of constant mass. This has the advantage of removing some of the uncertainties in the mass loss rate, convection theory, rotationally-induced mixing, and binary mass exchange which affect the final helium core mass as a function of main sequence mass.

After this, full star models along with the hydrogen envelope are considered. According to the author, the envelope does not affect the hydrodynamics of the helium cores but is very important if the correct light curves during these events are to be made sense of. Other subtle effects of including a H-envelope include increasing the mass of the bound remnant by a few solar masses and shortening the interval between pulses. With this in mind, various supernovae light curves are simulated and analysed.

A few other models of blue progenitors, stars with rotation, and superluminous supernovae are also considered for solar abundances. After this, there is a section where the author considers the possibility of Eta Carina as a PPISN in progress. The final section reviews the nucleosynthesis expected from PPISN.

8.1.18 Rotation, binaries, accretion-BHMG [40]

We study 4 effects here -

A change in the rate of the CO and increase in the rate for the triple-alpha

The rate of the CO reaction characterized by S factor, taken here to be between 110 and 205 keV. The rate for the 3α reaction depends on the radiative width for the “Hoyle state”, we define $f_{3\alpha}$ as the multiplier to the known rate, take max to be 1.35. Decreasing the rate of CO reaction or increasing for 3α , makes the explosion milder (more C), less matter ejected, affects final remnant mass a little, raise M_{low} from 46-56 M_0 . Large CO rates and low 3α rates PPISN evolution not very sensitive. Increasing 3α rate rise maximum to $64M_0$. Very extreme values unlikely due to nucleosynthesis constraints. Within same constraints, M_{high} varies from 136 – 161 M_0 .

Along with metallicity, they take into account single stars that retain part of their hydrogen envelopes when they die can produce more massive black holes. Can be as large as $90M_0$ with very low metallicity and mass loss.

Making the black hole in a detached binary

Can make an $85M_0$ black hole in an isolated star and later capture it in a binary, then there only needs to be one stage of capture, or can be made in a detached binary.

The effects of rapid rotation

For rotating stars, which experience chemically homogeneous evolution and lose less than 30% of their mass during hydrogen and helium burning (with low metallicities), including magnetic torques, M_{low} can go up to 70 M_0 . Effects of M_{high} are much lower.

Super Eddington accretion post black hole formation

Accretion post formation occurs either during the common envelope phase that is frequently invoked to bring the stars together or during frictionally-induced mass loss by the secondary after it finishes hydrogen burning. Considering envelope masses spilled over to the blackhole, and the usual thermal time scale, very high accretion rates are found. At these high rates, blackholes will accrete most of the matter, but also produce strong bipolar outflows.

8.1.19 GW190521 as a statistical outlier [26]

They study two phenomenological mass models (with mass ratio is given as a power law favoring equal mass binaries) -

- Broken Power Law: The primary mass distribution is characterized by a gentle sloping power law at low mass and a second steep sloping power law at high mass
- Power Law + Peak: The primary mass distribution is characterized by a power law component at low mass and wide Gaussian component at high masses

They study the cases of $m_1 < 40, 50, 65M_0$ to account for uncertainty in PPI gap. They generate batches of simulated events from the two models and compare GW190521 against the outlier from each batch.

For $m_1 < 65M_0$, they find the probability for the models to produce an outlier as significant as GW190521 to be less than 0.0001. GW190521 is identified as an outlier to both population models. The remaining BBH events are consistent with both models.

For $m_1 < 50M_0$, they find the probability for the models to produce an outlier as significant as GW190521 to be less than 0.0001. GW190521 is a clear outlier to both models. The next closest outlier lies just outside the 98% confidence interval. For the BPL_{50} model, GW190521 and the other are evaluated as potential outliers, and the remaining events are consistent with the population model. For the PLP_{50} model, only GW190521 is identified as an outlier, while the remaining

distribution of events are inconsistent with the model.

For $m_1 < 40M_\odot$, they find the probability for the models to produce an outlier as significant as GW190521 to be less than 0.0001. Two events — GW190521 and another, same as before — are found to be potential population outliers. The remaining 20 BBH events are inconsistent with both stellar-mass population models.

They conclude that if the PI mass gap begins at or below $65M_\odot$, then GW190521 is a clear outlier to the stellar-mass BBH population and that its outlier significance cannot be explained by statistical fluctuations. There is also some evidence that GW190706 222641 could be an outlier to the stellar-mass population if $PI < 50M_\odot$.

8.1.20 GW190521 as a straddling binary [12]

Rather than concluding that both components of GW190521 belong to a new population of mass-gap BHs, this paper explore the scenario in which GW190521's secondary mass (the lower one) belongs to the previously-observed population of BHs. When analyzed with uninformative priors, both component masses of GW190521 fall within the PISN mass gap.

They analyze this event with the population informed priors (assuming that a merger with at most one mass-gap BH is a priori more likely than a double mass-gap merger), and using existing population data to set a mass prior on the secondary BH, with the other one being on the far side of the mass gap. Thus they predict GW190521 to be a merger between a stellar BH and and IMBH. Thus, its more likely to be a straddling binary.

8.2 Particle Physics Papers

8.2.1 Beyond the Standard Model Explanations of GW190521 [31]

In this paper, the authors propose several explanations for GW190521 based on models of new physics. First they propose explanations through the Standard Model and find that it is a challenge for standard astrophysical theory as it leads to uncertainties of only $3 - 5M_\odot$ in the mass gap.

Beyond Standard Model explanations include:

- New particles: Lower edge of the mass gap was obtained for the case of energy loss due to hidden photons, photophilic axion, and the electrophilic axion.
- Large Extra Dimensions: They implemented the losses due to KK modes resulting from photon-photon annihilation, gravi-Compton-Primakoff scattering, and gravi-bremsstrahlung processes into MESA using the rates for n additional compactified spatial dimensions. With this they arrived at a lower edge for the mass gap.
- Neutrino magnetic moment: Increase in ν -magnetic moment in Beyond Standard Model scenarios causes coupling of photon to neutrinos resulting in additional neutrino loss channels. effects similar to new particles. The lower mass of the mass gap was obtained for this case too.
- Modified Gravity: Both the lower and upper edge of the mass gap was obtained for this scenario as changes in the gravitational constant G was examined. It was found that an increase in G moves both the edges to lower masses and vice versa.

8.2.2 Effect of Non-Nuclear Energy on BHMG [42]

They propose adding an energy source throughout the star in addition to nuclear fusion, it is possible for the altered evolution to avoid the complete destruction of a pair instability supernova, and instead a BH remnant is left behind. An example of an extra energy source is dark matter annihilation within the star, but their results hold more generally.

They show that when 50% of the stellar luminosity arises from the new heat source, the star is no longer completely destroyed. The function ϵ describes the amount of energy generated per unit time per unit mass within the star, including nuclear energy production, energy loss due to neutrinos and gravitational binding energy changes, and to this they add a constant energy source. Constancy is taken since weak dependence wrt T and ρ is usually the case with DM annihilation. The pair instability region $\Gamma < 4/3$ is unchanged.

They start with a $30M_{\odot}$ star seed and they gradually add mass and also the constant energy until target mass is reached. Here similarly the Riemann solver is called if $\int_0^M (\gamma - 4/3) P / \rho dM$ is negative. More the extra energy we add, more is the deviation away from instability.

8.3 Miscellaneous Papers

We would like to thank Aman Awasthi for his contribution in writing the summaries for the following papers.

8.3.1 Core-Collapse Supernovae from 9 to 120 Solar Masses Based on Neutrino-powered Explosions [34]

- For supernovae resulting from massive stars with solar metallicity and masses from $9.0 M_{\odot}$ to $120 M_{\odot}$ they calculated the following properties: **nucleosynthesis, light curves, explosion energies, and remnant masses**.
- The models under study are one dimensional, of a single metallicity, and do not include any effects by rotation.
- In their survey, they are using a one-dimensional neutrino transport model for the explosion and then they are calibrating this model to give the observed energy for SN 1987A, using five standard progenitors, and for the Crab supernova using a $9.6 M_{\odot}$ progenitor. Some of their findings are:
 - The final kinetic energy of the supernova is variable and sensitive to the structure of each presupernova star.
 - Several progenitors with extended core structures do not explode, but become black holes, and the masses of exploding stars do not form a continuous range.
 - the resulting NS(neutron star) IMF has a mean gravitational mass near $1.4 M_{\odot}$.
 - The average BH mass is about $9 M_{\odot}$ if only the helium core implodes, and $14 M_{\odot}$, if the entire presupernova star collapses.

8.3.2 Constraints on Core Collapse from the Black Hole Mass function[18]

Used approximation: The observed black hole mass function is under the assumption that black hole formation is controlled by the compactness of the stellar core at the time of collapse.

Results: They find that the compactness $\xi_{2.5}$ above which 50% of core collapses produce black

holes is $\xi_{2.5}^{50\%} = 0.24(0.15 < \xi_{2.5}^{50\%} < 0.37 \text{ at } 90\% \text{ confidence})$.

The models also predict that $f = 0.18(0.09 < f < 0.39)$ of core collapses fail.

Out of four other criteria for black hole formation based on $\xi_{2.0}$ (the compactnesses at enclosed mass of $2.0M_{\odot}$) and $\xi_{3.0}$ (the compactnesses at enclosed mass of $3.0M_{\odot}$) rather than $2.0M_{\odot}$, the mass of the iron core M_{Fe} , and the mass inside the oxygen burning shell M_O , They found that $2.0M_{\odot}$ works as well as $2.5M_{\odot}$, while $3.0M_{\odot}$, M_{Fe} and M_O are not useful.

Claim: As expected from the high compactness of 20–25 M_{\odot} stars, black hole formation in this mass range provides a natural explanation of the red supergiant problem

8.3.3 How Massive Single Stars End their Life [15]

This is a completely theoretical paper that starts out with the assumptions of stellar structure theory by giving an overview of stellar models and paradigms, mass loss (through a simplified prescription of the effect of metallicity), and the properties of stellar remnants (mapped as a function of mass and metallicity). It then explains the various types of supernovae including Type IIp, IIL, Ib, Ic supernovae, Nickel-deficient supernovae, pair-instability supernovae, jet-powered supernovae, Gamma Ray bursts, and collapsars.

Integrating over an initial mass function, the authors derive the relative populations of supernovae as a function of metallicity. They also examine uncertainties in mass loss, explosion mechanisms, and the effects of rotation and its possible consequences.

8.3.4 Effect of PI Mass Loss on Mergers[3]

This not a very new paper. It was released in 2016. Until then, pair-instability pulsation supernovae had been neglected in the modelling of BH mergers. PISN associated with severe mass loss may suppress the formation of massive BHs, decreasing BH merger rates for the highest BH masses. The paper aims to address this issue by probing the (classical hydrodynamical) effects of this on merger rate and mass using populations of double black hole binaries with mass loss incorporated into the StarTrack population synthesis code.

The paper contains an overview of pair-instability pulsations/ supernovae and a detailed description of their population synthesis model, calculations, and incorporation into StarTrack. With this, they obtain the mass gap as 50-135 M_{\odot} and the total intrinsic merger mass distribution (not much difference was noticed in this with/without PPISN except at lower metallicities). The authors also arrive at a prediction of the number of BH-BH mergers during a section of the LIGO-VIRGO observation run and conclude that an observation of a progenitor BH of mass $> 50M_{\odot}$ would require the consideration of new physics.

8.3.5 Observational constraints on the progenitors of core-collapse supernovae : the case for missing high mass stars[32]

- It is a review article on identify progenitor stars of core-collapse supernovae discovered in nearby galaxies.

- He compiles these results (from 1999 - 2013) in a distance limited sample and discusses the implications of the findings. The data for 45 supernovae progenitors illustrate a remarkable deficit of high luminosity stars above an apparent limit of $\log L/L_{\odot} \simeq 5.1$ dex (a dex is simply an order of magnitude).
- By Salpeter initial mass function, one would expect to have found 13 high luminosity and high mass progenitors by the writing of this paper (May 2015). Possibly, only one object in the taken time and volume limited sample is unambiguously high mass (the progenitor of SN2009ip) although the nature of that supernovae was debated on that time.
- The possible biases like circumstellar dust, the luminosity analysis, and sample selection methods are reviewed but these can explain the missing high mass progenitor stars.
- Theoretical explosions of model stars predict that black hole formation and failed supernovae tend to occur above an initial mass of $M \simeq 18 M_{\odot}$ but in till 2015, there was not any observed progenitor of mass greater than $18 M_{\odot}$.
- The observational constraints are quite consistent with the bulk of stars above $M > 18 M_{\odot}$ collapsing to form black holes with no visible supernovae

8.3.6 Progenitor Mass Distribution of Core-Collapse Supernova Remnants in Our Galaxy and Magellanic Clouds based on Elemental Abundances [16]

- They count the number of CC-SNRs in three mass ranges
 $A : M_{ZAMS} < 15 M_{\odot}$,
 $B : 15 M_{\odot} < M_{ZAMS} < 22.5 M_{\odot}$,
 $C : M_{ZAMS} > 22.5 M_{\odot}$,
- Simple compilation of progenitor masses in the literature gives a progenitor mass distribution of $f_A : f_B : f_C = 0.24 : 0.28 : 0.48$, here f is the number fraction of the progenitors. **The distribution is inconsistent with any standard initial mass functions.**
- The above mass estimates have large systematic uncertainties because most of the relative abundances (X/Si) are not really good probe for the progenitor masses.
- They propose to rely only on the Fe/Si ratio which is sensitive to the CO core mass $M_{CO \text{ core}}$ and M_{ZAMS} .
- Using the Fe/Si ratio, and the newest theoretical model, they estimated 33 $M_{CO \text{ core}}$ and M_{ZAMS} which leading to a revised progenitor mass distribution of $f_A : f_B : f_C = 0.47 : 0.32 : 0.21$. **This is consistent with the standard Salpeter initial mass function.**
- The relation between $M_{CO \text{ core}}$ and M_{ZAMS} may be affected by binary evolution, which is not considered in their study, so to get a better estimate of progenitor mass distribution it should be considered in the future work.

8.3.7 Stellar Collapse Diversity and the Diffuse Supernova Neutrino Background [20]

- A detailed analysis on the diffuse cosmic supernova neutrino background (DSNB) is done. It is the observational target of the gadolinium-loaded Super-Kamiokande detector Hyper-Kamiokande detectors.

- The current predictions for DSNB are hampered by the supernova explosion mechanism and of the neutron star equation of state and maximum mass. In this paper DSNB problem is reviewed on the basis of the landscapes of successful and failed SN explosions, with parametrized one dimensional neutrino engines for large sets of single-star and helium-star progenitors.
- Besides considering engines of different strengths leading to different fractions of failed SNe with black-hole (BH) formation, They are
 - varying the NS mass limit,
 - varying the spectral shape of the neutrino emission,
 - including the contributions from poorly understood alternative NS-formation channels such as accretion-induced or merger-induced collapse events.
- Their predictions are higher than other recent ones because they are including a large fraction of failed SNe with long delay to BH formation.
- Some results of their best-guess model predicts a DSNB $\bar{\nu}_e$ flux of $28.8^{+24.6}_{-10.9}\text{cm}^{-2}\text{s}^{-1}$, with $6.0^{+5.1}_{-2.1}\text{cm}^{-2}\text{s}^{-1}$ in the interval of $[10, 30]\text{MeV}$ and $1.3^{+1.1}_{-0.4}\text{cm}^{-2}\text{s}^{-1}$ with $\bar{\nu}_e > 17.3\text{MeV}$.
Just to comparison, for Super-Kamiokande, DSNB $\bar{\nu}_e$ flux with $\bar{\nu}_e > 17.3\text{MeV}$ is $2.7\text{cm}^{-2}\text{s}^{-1}$ at 90%CL. The above predicted value by the authors is roughly two factors lower than this limit.
- The differential number flux of DSNB neutrinos or antineutrinos, isotropically flooding the Earth is computed as the line-of-sight integral of the IMF-weighted neutrino spectrum of past core-collapse events multiplied by the comoving core-collapse rate density over the cosmic history.

8.3.8 The Black Hole formation probability[5]

- They have introduced a new paradigm for studying the final phases of a massive star's evolution: **a probabilistic description of BH formation**. It is different from the complicated relationship between M_{ZAMS} and NS or BH formation.
- Presently, the observational constraints on $P_{BH}(M_{ZAMS})$ are too weak for us to make firm, quantitative predictions about its nature.
- They have explained the concept of probabilistic BH formation by deriving three possible forms of $P_{BH}(M_{ZAMS})$. These are consistent with the weak constraints of the BH mass distribution and the level of chemical enrichment refer to massive stars.
- Under the probabilistic BH formation scenario, the relative numbers of NS–NS, BH–NS, BH–BH binaries, as well as the expected mass and mass ratio distributions amongst these binaries, could differ from the current predictions.
- The shape of the BH formation probability function will also determine the relative numbers of BHs and NSs, and the rate of unnoae (Unnova is the event when the observational signature of the birth of a black hole is the disappearance of a star rather than a nova).

8.3.9 The Search for Failed Supernovae with The Large Binocular Telescope: First Candidates[13]

- They are monitoring 27 galaxies within 10 Mpc using the Large Binocular Telescope to search for failed supernovae (SNe).
(Failed Supernova: a massive stars that collapse to form a black hole without a SN explosion)
- They also search for the low luminosity, long duration transients for failed explosions of red supergiants.
- After analyzing 4 years of data in direct search for failed SNe, they have one candidate which require further study. This candidate has an estimated mass of $18\text{--}25 M_{\odot}$, if real, implies that failed SN represent a median fraction of $f \simeq 0.30$ of core-collapses, with symmetric 90% confidence limits of $0.07 \leq f \leq 0.62$.
- As the duration of the survey increases, it will begin to constrain the $f \simeq 10 - 30\%$ failure rates needed to explain the deficit of massive SN progenitors and the observed black hole mass function.

8.3.10 The Deaths of Very Massive Stars[41]

The basic theory for the evolution of heavier stars ($\geq 10M_{\odot}$) is reviewed.

- Main sequence ($8M_{\odot} \leq M \leq 30M_{\odot}$) **or** helium core masses upto $12M_{\odot} \rightarrow$ iron core collapse to Neutron Stars leading to explosions that make today's observable supernovae.
- Main sequence ($8M_{\odot} \leq M \leq 30M_{\odot}$) **or** helium core masses $7 < M_{\odot}M < 12M_{\odot} \rightarrow$ iron core collapse to NS leading to explosions that make today's observable supernovae.
- Main sequence ($30M_{\odot} \leq M \leq 80M_{\odot}$) **or** helium core masses $10 < M_{\odot}M < 35M_{\odot} \rightarrow$ BH.
- Main sequence ($80M_{\odot} \leq M \leq 150M_{\odot}$) **or** helium core masses $35 < M_{\odot}M < 63M_{\odot} \rightarrow$ PPISN.
- Main sequence ($150M_{\odot} \leq M \leq 260M_{\odot}$) **or** helium core masses $63 < M_{\odot}M < 133M_{\odot} \rightarrow$ PISN.
- Main sequence ($M \geq 260M_{\odot}$) **or** helium core masses $M_{\odot}M > 35M_{\odot} \rightarrow$ BH.

Apart from this some of important aspect discussed in the paper is as follows;

- The importance of compactness on the outcome of the stars is discussed. **compactness parameter** is defined as $\xi_{2.5} = 2.5/R_{2.5}$ is a quantitative measure of the density fall off. Here $R_{2.5}$ is the radius, in units of 1000 km, of the mass shell in the presupernova star that encloses $2.5M_{\odot}$.
- The fate of heavier stars is given in enough detail. The PISN and PPISN conditions are explored with additional effects like metallicity, rotation effect.
- The effect of rotation on the evolution of stars is explored pretty well. The scenarios of magnetars, GRBs are also explained.

References

- [1] R. Abbott, T.D. Abbott, S. Abraham, F. Acernese, K. Ackley, C. Adams, R.X. Adhikari, V.B. Adya, C. Affeldt, M. Agathos, and et al. Gw190521: A binary black hole merger with a total mass of 150m. *Physical Review Letters*, 125(10), Sep 2020.
- [2] Eric J. Baxter, Djuna Croon, Samuel D. McDermott, and Jeremy Sakstein. Find the gap: Black hole population analysis with an astrophysically motivated mass function. *The Astrophysical Journal Letters*, 916(2):L16, Jul 2021.
- [3] K. Belczynski, A. Heger, W. Gladysz, A. J. Ruiter, S. Woosley, G. Wiktorowicz, H.-Y. Chen, T. Bulik, R. O’Shaughnessy, D. E. Holz, and et al. The effect of pair-instability mass loss on black-hole mergers. *Astronomy Astrophysics*, 594:A97, Oct 2016.
- [4] Bradley W. Carroll and Dale A. Ostlie. *An Introduction to Modern Astrophysics*. 2nd (international) edition, 2007.
- [5] Drew Clausen, Anthony L. Piro, and Christian D. Ott. The black hole formation probability. *The Astrophysical Journal*, 799(2):190, Jan 2015.
- [6] Guglielmo Costa, Alessandro Bressan, Michela Mapelli, Paola Marigo, Giuliano Iorio, and Mario Spera. Formation of gw190521 from stellar evolution: the impact of the hydrogen-rich envelope, dredge-up, and 12c(,)16o rate on the pair-instability black hole mass gap. *Monthly Notices of the Royal Astronomical Society*, 501(3):4514–4533, Dec 2020.
- [7] Djuna Croon, Samuel D. McDermott, and Jeremy Sakstein. New physics and the black hole mass gap. *Physical Review D*, 102(11), Dec 2020.
- [8] V. De Luca, V. Desjacques, G. Franciolini, P. Pani, and A. Riotto. Gw190521 mass gap event and the primordial black hole scenario. *Phys. Rev. Lett.*, 126:051101, Feb 2021.
- [9] R.J. deBoer, J. Görres, M. Wiescher, R.E. Azuma, A. Best, C.R. Brune, C.E. Fields, S. Jones, M. Pignatari, D. Sayre, and et al. The c12(,)o16 reaction and its implications for stellar helium burning. *Reviews of Modern Physics*, 89(3), Sep 2017.
- [10] R. Farmer, M. Renzo, S. E. de Mink, P. Marchant, and S. Justham. Mind the gap: The location of the lower edge of the pair-instability supernova black hole mass gap. *The Astrophysical Journal*, 887(1):53, Dec 2019.
- [11] Rodrigo Fernández, Eliot Quataert, Kazumi Kashiyaama, and Eric R Coughlin. Mass ejection in failed supernovae: variation with stellar progenitor. *Monthly Notices of the Royal Astronomical Society*, 476(2):2366–2383, Feb 2018.
- [12] Maya Fishbach and Daniel E. Holz. Minding the gap: Gw190521 as a straddling binary. *The Astrophysical Journal*, 904(2):L26, Nov 2020.
- [13] J. R. Gerke, C. S. Kochanek, and K. Z. Stanek. The search for failed supernovae with the large binocular telescope: first candidates. *Monthly Notices of the Royal Astronomical Society*, 450(3):3289–3305, May 2015.
- [14] M. J. Graham, K. E. S. Ford, B. McKernan, N. P. Ross, D. Stern, K. Burdge, M. Coughlin, S. G. Djorgovski, A. J. Drake, D. Duev, M. Kasliwal, A. A. Mahabal, S. van Velzen, J. Belecki, E. C. Bellm, R. Burruss, S. B. Cenko, V. Cunningham, G. Helou, S. R. Kulkarni, F. J. Masci,

- T. Prince, D. Reiley, H. Rodriguez, B. Rusholme, R. M. Smith, and M. T. Soumagnac. Candidate electromagnetic counterpart to the binary black hole merger gravitational-wave event s190521g. *Phys. Rev. Lett.*, 124:251102, Jun 2020.
- [15] A. Heger, C. L. Fryer, S. E. Woosley, N. Langer, and D. H. Hartmann. How massive single stars end their life. *The Astrophysical Journal*, 591(1):288–300, Jul 2003.
 - [16] Satoru Katsuda, Tomoya Takiwaki, Nozomu Tominaga, Takashi J. Moriya, and Ko Nakamura. Progenitor mass distribution of core-collapse supernova remnants in our galaxy and magellanic clouds based on elemental abundances. *The Astrophysical Journal*, 863(2):127, Aug 2018.
 - [17] Tomoya Kinugawa, Takashi Nakamura, and Hiroyuki Nakano. Formation of binary black holes similar to gw190521 with a total mass of 150 m from population iii binary star evolution. *Monthly Notices of the Royal Astronomical Society: Letters*, 501(1), Dec 2020.
 - [18] C. S. Kochanek. Constraints on core collapse from the black hole mass function. *Monthly Notices of the Royal Astronomical Society*, 446(2):1213–1222, Nov 2014.
 - [19] Kyle Kremer, Mario Spera, Devin Becker, Sourav Chatterjee, Ugo N. Di Carlo, Giacomo Fragione, Carl L. Rodriguez, Claire S. Ye, and Frederic A. Rasio. Populating the upper black hole mass gap through stellar collisions in young star clusters. *The Astrophysical Journal*, 903(1):45, Oct 2020.
 - [20] Daniel Kresse, Thomas Ertl, and Hans-Thomas Janka. Stellar collapse diversity and the diffuse supernova neutrino background. *The Astrophysical Journal*, 909(2):169, Mar 2021.
 - [21] P. Ledoux. On the Radial Pulsation of Gaseous Stars. , 102:143, September 1945.
 - [22] P. Ledoux. On the Dynamical Stability of Stars. , 104:333, November 1946.
 - [23] Shing-Chi Leung, Ken’ichi Nomoto, and Sergei Blinnikov. Pulsational pair-instability supernovae. i. pre-collapse evolution and pulsational mass ejection. *The Astrophysical Journal*, 887(1):72, Dec 2019.
 - [24] Pablo Marchant and Takashi J. Moriya. The impact of stellar rotation on the black hole mass-gap from pair-instability supernovae. *Astronomy Astrophysics*, 640:L18, Aug 2020.
 - [25] M. R. Mokiem, A. de Koter, J. S. Vink, J. Puls, C. J. Evans, S. J. Smartt, P. A. Crowther, A. Herrero, N. Langer, D. J. Lennon, and et al. The empirical metallicity dependence of the mass-loss rate of o- and early b-type stars. *Astronomy Astrophysics*, 473(2):603–614, Aug 2007.
 - [26] Brendan O’Brien, Marek Szczepanczyk, V. Gayathri, Imre Bartos, Gabriele Vedovato, Giovanni Prodi, Guenakh Mitselmakher, and Sergey Klimentko. Detection of ligo-virgo binary black holes in the pair-instability mass gap, 2021.
 - [27] Seth Olsen, Javier Roulet, Horng Sheng Chia, Liang Dai, Tejaswi Venumadhav, Barak Zackay, and Matias Zaldarriaga. Mapping the likelihood of gw190521 with diverse mass and spin priors, 2021.
 - [28] Bill Paxton, Josiah Schwab, Evan B. Bauer, Lars Bildsten, Sergei Blinnikov, Paul Duffell, R. Farmer, Jared A. Goldberg, Pablo Marchant, Elena Sorokina, and et al. Modules for experiments in stellar astrophysics (**mesa**): Convective boundaries, element diffusion, and massive star explosions. *The Astrophysical Journal Supplement Series*, 234(2):34, Feb 2018.

- [29] Jade Powell, Bernhard Müller, and Alexander Heger. The final core collapse of pulsational pair instability supernovae. *Monthly Notices of the Royal Astronomical Society*, 503(2):2108–2122, Mar 2021.
- [30] M Renzo, R J Farmer, S Justham, S E de Mink, Y Götzberg, and P Marchant. Sensitivity of the lower edge of the pair-instability black hole mass gap to the treatment of time-dependent convection. *Monthly Notices of the Royal Astronomical Society*, 493(3):4333–4341, Mar 2020.
- [31] Jeremy Sakstein, Djuna Croon, Samuel D. McDermott, Maria C. Straight, and Eric J. Baxter. Beyond the standard model explanations of gw190521. *Physical Review Letters*, 125(26), Dec 2020.
- [32] S. J. Smartt. Observational constraints on the progenitors of core-collapse supernovae: The case for missing high-mass stars. *Publications of the Astronomical Society of Australia*, 32, 2015.
- [33] Maria C. Straight, Jeremy Sakstein, and Eric J. Baxter. Modified gravity and the black hole mass gap. *Physical Review D*, 102(12), Dec 2020.
- [34] Tuguldur Sukhbold, T. Ertl, S. E. Woosley, Justin M. Brown, and H.-T. Janka. Core-collapse supernovae from 9 to 120 solar masses based on neutrino-powered explosions. *The Astrophysical Journal*, 821(1):38, Apr 2016.
- [35] Ataru Tanikawa, Tomoya Kinugawa, Takashi Yoshida, Kotaro Hijikawa, and Hideyuki Umeda. Population iii binary black holes: effects of convective overshooting on formation of gw190521. *Monthly Notices of the Royal Astronomical Society*, 505(2):2170–2176, May 2021.
- [36] Hideyuki Umeda, Takashi Yoshida, Chris Nagele, and Koh Takahashi. Pulsational pair-instability and the mass gap of population iii black holes: Effects of overshooting. *The Astrophysical Journal*, 905(2):L21, Dec 2020.
- [37] L. A. C. van Son, S. E. De Mink, F. S. Broekgaarden, M. Renzo, S. Justham, E. Laplace, J. Morán-Fraile, D. D. Hendriks, and R. Farmer. Polluting the pair-instability mass gap for binary black holes through super-eddington accretion in isolated binaries. *The Astrophysical Journal*, 897(1):100, Jul 2020.
- [38] Jorick S Vink, Erin R Higgins, Andreas A C Sander, and Gautham N Sabhahit. Maximum black hole mass across cosmic time. *Monthly Notices of the Royal Astronomical Society*, 504(1):146–154, Mar 2021.
- [39] S. E. Woosley. Pulsational pair-instability supernovae. *The Astrophysical Journal*, 836(2):244, Feb 2017.
- [40] S. E. Woosley and Alexander Heger. The pair-instability mass gap for black holes. *The Astrophysical Journal Letters*, 912(2):L31, May 2021.
- [41] Stan. E. Woosley and Alexander Heger. The deaths of very massive stars. *Astrophysics and Space Science Library*, page 199–225, Sep 2014.
- [42] Joshua Ziegler and Katherine Freese. Filling the black hole mass gap: Avoiding pair instability in massive stars through addition of nonnuclear energy. *Physical Review D*, 104(4), Aug 2021.